



# Non-intrusive Human Vital Sign Detection Using mmWave Sensing Technologies: A Review

YINGXIAO WU, HAOCHENG NI, CHANLIN MAO, and JIANPING HAN, Hangzhou Dianzi University, China  
WENYAO XU, University at Buffalo, USA

Non-invasive human vital sign detection has gained significant attention in recent years, with its potential for contactless, long-term monitoring. Advances in radar systems have enabled non-contact detection of human vital signs, emerging as a crucial area of research. The movements of key human organs influence radar signal propagation, offering researchers the opportunity to detect vital signs by analyzing received electromagnetic (EM) signals. In this review, we provide a comprehensive overview of the current state-of-the-art in millimeter-wave (mmWave) sensing for vital sign detection. We explore human anatomy and various measurement methods, including contact and non-contact approaches, and summarize the principles of mmWave radar sensing. To demonstrate how EM signals can be harnessed for vital sign detection, we discuss four mmWave-based vital sign sensing (MVSS) signal models and elaborate on the signal processing chain for MVSS. Additionally, we present an extensive review of deep learning-based MVSS and compare existing studies. Finally, we offer insights into specific applications of MVSS (e.g., biometric authentication) and highlight future research trends in this domain.

CCS Concepts: • Human-centered computing → Ubiquitous and mobile computing;

Additional Key Words and Phrases: Vital sign, non-intrusive, mmWave radar, mmWave sensing, sensing models

## ACM Reference format:

Yingxiao Wu, Haocheng Ni, Changlin Mao, Jianping Han, and Wenya Xu. 2023. Non-intrusive Human Vital Sign Detection Using mmWave Sensing Technologies: A Review. *ACM Trans. Sensor Netw.* 20, 1, Article 16 (November 2023), 36 pages.

<https://doi.org/10.1145/3627161>

## 1 INTRODUCTION

In recent years, the demand for non-contact vital sign monitoring has surged, leading to rapid market growth. A report by Fortune Business Insights [1] states that the global remote patient monitoring devices market size reached USD 25.32 billion in 2020, exhibiting substantial growth of 48.5% compared to 2017–2019. Furthermore, the global remote patient monitoring devices market is projected to reach USD 101.02 billion by 2028.

---

This research was supported by Zhejiang Provincial Natural Science Foundation of China under Grant No.LY23F010009. Authors' addresses: Y. Wu, H. Ni, C. Mao, and J. Han, Hangzhou Dianzi University, Hangzhou, China; e-mails: wuyingxiao@hdu.edu.cn, ni\_haocheng@hdu.edu.cn, mao.cl@hdu.edu.cn, hanjp@hdu.edu.cn; W. Xu, University at Buffalo, Buffalo, NY; e-mail: wenyaoxu@buffalo.edu.

Permission to make digital or hard copies of all or part of this work for personal or classroom use is granted without fee provided that copies are not made or distributed for profit or commercial advantage and that copies bear this notice and the full citation on the first page. Copyrights for components of this work owned by others than the author(s) must be honored. Abstracting with credit is permitted. To copy otherwise, or republish, to post on servers or to redistribute to lists, requires prior specific permission and/or a fee. Request permissions from [permissions@acm.org](mailto:permissions@acm.org).

© 2023 Copyright held by the owner/author(s). Publication rights licensed to ACM.

1550-4859/2023/11-ART16 \$15.00

<https://doi.org/10.1145/3627161>

The COVID-19 pandemic and the growing prevalence of chronic diseases such as cardiovascular diseases and diabetes are the two main factors fueling the rapid growth of the vital sign monitoring market. As of late March 2022, COVID-19 has resulted in over 6.1 million deaths and nearly 481 million infections worldwide [2]. Medical professionals face a high risk of infection, and non-contact methods for remote patient vital sign monitoring can help minimize the risk associated with close contact. Chronic diseases are responsible for 71% of all global deaths, claiming 41 million lives annually [3]. Continuous monitoring of vital signs for patients with chronic illnesses is essential, and non-contact approaches offer benefits such as being unintrusive and suitable for long-term monitoring. Applications for non-contact vital sign monitoring extend beyond the medical field and include the automotive industry [4] (monitoring driver's vital signs for safe driving), emergency rescue [5], biometric authentication [6], and emotion recognition [7], among others.

Recent advancements in radar technologies and sensing methodologies have led to numerous researchers worldwide working on developing signal acquisition and processing approaches. These topics cover a wide range, including heartbeat detection, respiration rate detection, sleep monitoring, multi-resident detection, and signal processing platforms, among others. Several recent surveys on wireless human sensing are discussed below.

Tran et al. [8] examined traditional sleep monitoring techniques (e.g., polysomnography) and the current state and challenges of radar-based sleep monitoring technology, while indicating the current challenges and commercialization direction of radar sleep monitoring technology. Leonhardt et al. [9] specifically explored technologies for contactless monitoring of human vital signs in automotive environments. Cardillo et al. [10] conducted an extensive survey on vital sign detection and human localization using **multiple-input multiple-output (MIMO)** radar. Kebe et al. [11] offered a thorough review of traditional cardio-pulmonary rate monitoring methods and highlighted the challenges faced by radar-based vital sign monitoring approaches. Two additional reviews focus on radar hardware. Singh et al. [12] detailed the primary challenges associated with hardware and signal processing algorithms for vital sign monitoring using radar, summarizing the directions and challenges for multi-person monitoring. Obadi et al. [13] reviewed recent developments in radar-based vital signs detection, with a special emphasis on signal-processing platforms and algorithm implementation using FPGAs. Paterniani et al. [14] provided an overview of existing radar signal processing algorithms and radar systems developed for the estimation of vital signs and pointed out the most relevant trends in current research activities on radar systems for vital signs monitoring. Zhang et al. [15] reviewed the current state-of-the-art of mmWave-based human sensing tasks with different sensing granularities, e.g., human localization, activity recognition, and vital monitoring. They further discussed potential challenges and future directions, including hardware and platforms, enhanced applicability, new sensing schemes, and so on.

In comparison to the recent reviews mentioned earlier, our review article offers the following unique contributions:

- We present an extensive review of the current state-of-the-art in mmWave radar technology for vital sign detection, covering topics from mmWave waveforms, MVSS signal models, and signal processing algorithms to deep learning-based MVSS and system implementation.
- We provide a detailed review of four MVSS signal models and their principles for vital sign detection.
- We discuss the MVSS signal processing chain and compare different algorithms for estimating **heart rate (HR)**, **respiratory rate (RR)**, and **blood pressure (BP)**.
- To the best of our knowledge, our article is the first to offer an overview of publications that utilize deep learning in the field of MVSS.

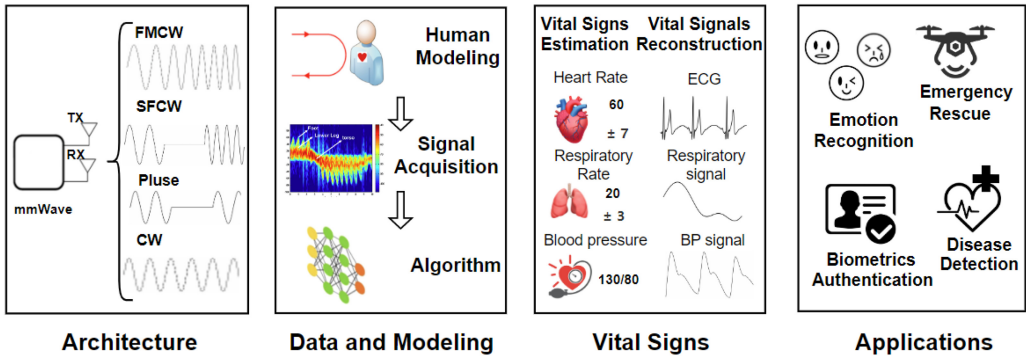


Fig. 1. The review framework.

The remaining structure of this review article is organized as follows: Section 2 discusses physiological parameters-related topics, including human anatomy and measurement methods. Section 3 provides an overview of the history, features, and applications of mmWave technologies. Section 4 details four MVSS signal models. In Section 5, we propose the MVSS signal processing chain. Section 6 reviews deep learning-based MVSS studies. Finally, Section 7 presents discussions and conclusions. Figure 1 shows the framework of this survey research. To facilitate easy reading, we provide a list of most abbreviations used throughout the manuscript in Table 1.

## 2 VITAL SIGNS AND MEASUREMENT METHODS

Vital signs refer to a collection of physiological parameters that represent the physical and mental condition of a person. Essential vital signs monitoring for medical and healthcare purposes typically consist of **Heart Rate (HR)**, **Respiratory Rate (RR)**, and **Blood Pressure (BP)**. These vital signs play a crucial role in various applications, such as evaluating heart rate variability, detecting early signs of sleep apnea, and serving as security authentication measures.

### 2.1 Heart Rate

Physiologically, the heart is located in the middle mediastinum on the left side of the chest [16]. It is composed of four chambers (the upper two atria receive blood, while the lower two ventricles pump blood into the lungs and arteries) and four valves that ensure blood flows in the correct direction [16, 17]. Figure 2 illustrates the changes in heart morphology, blood flow, and **electrocardiogram (ECG)** signal during various stages of a cardiac cycle, which includes systole and diastole. The QRS complex of the ECG signals the start of ventricular contraction. During systole, deoxygenated and oxygenated blood is expelled from the right and left ventricles, through the pulmonary arteries and aorta, into the lungs and arterial system, respectively. The end of the T wave indicates the onset of ventricular diastole. In diastole, deoxygenated and oxygenated blood is transported via the superior/inferior vena cava and pulmonary veins to the right and left atrium, respectively. Until the appearance of P waves and atrial contraction, deoxygenated and oxygenated blood is transferred from the right and left atria, respectively, into the right and left ventricles.

HR represents the number of heartbeats per time unit, typically expressed in **beats per minute (BPM)**. For healthy resting adults, the HR ranges from 54 to 100 bpm (0.9–1.67 Hz) [18]. Abnormal HR could indicate early signs of cardiovascular diseases, such as bradycardia (HR below the normal range) and tachycardia (HR above the normal rate) [19]. When accurate heartbeat intervals are obtained, **heart rate variability (HRV)** can be calculated as the time variation between consecutive heartbeat intervals. As shown in Figure 2, when using ECG to assess HRV, the R-R interval (time

Table 1. Table of Abbreviations Defined in the Article

Abbreviations	Full name	Abbreviations	Full name
MVSS	mmWave-based Vital Sign Sensing	MIMO	Multiple Input Multiple Output
HR	Heart Rate	RR	Respiratory Rate
BP	Blood Pressure	ECG	electrocardiogram
HRV	Heart Rate Variability	BPM	Beats Per Minute
PCG	Phonocardiography	SCG	Seismocardiography
PPG	Photoplethysmography	LVD	Laser Doppler Vibrometer
CW	continuous wave	IR-UWB	Impulse Radio Ultra Wideband
FMCW	Frequency Modulated Continuous Wave	VCO	Voltage Controlled Oscillator
SFCW	Stepped Frequency Continuous Wave	ACF	Autocorrelation Function
RSSI	Received Signal Strength Indicator	CSI	Channel State Information
SNR	Signal-to-Noise Ratio	ADC	Analog-to-Digital Converter
LPF	Lowpass Filter	IF signal	Intermediate Frequency signal
SIL radar	Self-Injection-Locked radar	SILO	SIL Oscillator
EM	Electromagnetic	FFT	Fast Fourier Transform
FoV	Field of View	DC	Direct Current
DOA	Direction of Arrival	MVDR	Minimum Variance Distortionless Response
LCMV	Linearly Constrained Minimum Variance	MUSIC	Multiple Signal Classification
BPF	Bandpassing Filter	CFAR	Constant False Alarm Rate
LMS Filter	Least Mean Square Filter	EMD	Empirical Mode Decomposition
VMD	Variational Mode Decomposition	CS-OMP	Compressive Sensing based on Orthogonal Matching Pursuit
CaSE	Cardiac-mmWave Scattering Effect	PCA	Principal Component Analysis
CWT	Continuous Wavelet Transform	IBI	Inter-Beat Interval
PWV	Pulse Wave Velocity	PTT	Pulse Transit Time
LSTM	Long Short Term Memory	SVM	Support Vector Machine
CNN	Convolutional Neural Network	VED	Variational Encoder-Decoder
SVD	Singular Value Decomposition	IFFT	inverse Fast Fourier Transform
CIR	Channel Impulse Response	KNN	K-Nearest Neighbor
ESPRIT	Estimation of Signal Parameters via Rotational Invariance Techniques	CEEMDAN	Complete Ensemble Empirical Mode Decomposition with Adaptive Noise

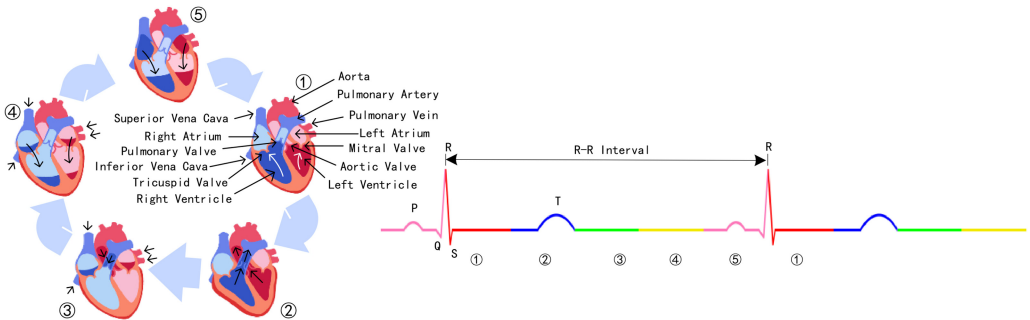


Fig. 2. Anatomy of a human heart as well as the association between ECG signal and cardiac events. Brief description of cardiac cycle phases 1 to 5: ventricular contraction pushes tricuspid and mitral valves closed; blood is ejected when pulmonary and aortic valves open; tricuspid and mitral valves close, then blood flows into atria; chambers relax and blood fills ventricles passively; atrial contraction forces blood into ventricles.

between two successive R-waves) is typically considered the heartbeat interval. Due to the valuable information HRV provides about the autonomic nervous system and heart health, it is used for diagnosing cardiovascular diseases [20], emotion recognition [7], and stress assessment [21], among other applications.

## 2.2 Respiratory Rate

According to human anatomy, the lungs are situated in the chest on either side of the heart within the rib cage [22], facilitating gas exchange. Specifically, when the diaphragm (the partition separating the chest and abdominal cavities) contracts, the chest cavity expands and negative pressure is produced, drawing air containing oxygen into the lungs [23]. The exchange of oxygen and carbon dioxide occurs at the respiratory membrane, where alveolar and capillary walls converge. Finally, when the thoracic diaphragm relaxes and positive pressure is generated, air containing carbon dioxide is expelled through the nose or mouth. This process constitutes a breathing cycle. **Respiratory rate (RR)** is the frequency of breaths within a specific time period. For healthy resting adults, the RR ranges from 6 to 20 BPM (0.1–0.33 Hz) [18]. As a result, abnormal breathing patterns can be identified by measuring RR, such as bradypnea (RR below the normal range), tachypnea (RR above the normal range), and apnea (respiratory arrest) [24].

## 2.3 Blood Pressure

BP is the force exerted by circulating blood against the walls of blood vessels and serves as a crucial indicator associated with cardiovascular disease [25]. BP is typically represented as systolic pressure over diastolic pressure, with measurements taken during distinct phases of the cardiac cycle. Systolic pressure is recorded when the left ventricle contracts, forcing blood out and causing BP to peak. Diastolic pressure is documented when the left ventricle relaxes and BP is at its lowest point. For healthy resting adults, BP ranges between 90/60 and 140/90 mmHg (millimeters of mercury above the ambient atmospheric pressure) [26]. Abnormal BP suggests a potential risk of cardiovascular diseases, such as hypotension (BP below the normal range) and hypertension (BP exceeding the normal range).

## 2.4 Measurement Methods

To date, various conventional measurement methods have been developed to monitor vital signs based on different physical signals and sensing technologies, such as ECG, **phonocardiography (PCG)**, **seismocardiography (SCG)**, and **photoplethysmography (PPG)**. These technologies enable vital sign recordings at different positions, such as the chest, fingertip, neck, and wrist.

ECG [27] uses 12-lead electrodes placed on the upper body to record the action potential of the cardiac electrical conduction system, reflecting myocardial contractions. ECG systems not only monitor cardiac events but also estimate RR based on breath-modulated ECG data [28]. PCG [29] monitors heart activity through heart sounds detected by a microphone. Heart sounds originate from vibrations in the myocardial wall resulting from the mechanical movements of the heart, such as the opening and closing of heart valves. SCG [30] records a human heart's mechanical vibrations using an accelerometer placed near the heart's apex to capture micro-vibrations of the chest wall. PPG [31] detects changes in blood flow volume in the vascular tree through optical means. As blood flow is regulated by neural, cardiac, and respiratory interactions, various physiological parameters such as HR, RR, and BP can theoretically be extracted from PPG signals.

Most traditional vital sign detection methods rely on sensors in contact with the body, which may cause discomfort, constrain subjects, and make long-term measurements impossible. Furthermore, they may result in skin damage, infection, or other adverse reactions in people with sensitive skin, such as neonates or burn victims. To address these issues, non-contact vital

Table 2. Comparison of Vital Sign Measurement Techniques

Methods	Working mode	Vital signs detected	Physical signal	Measuring sensor	Location	Drawbacks
ECG	Contacted	HR, RR	Electrical	Conductive electrode	Upper body	Motion artifacts
PCG	Contacted	HR	Sound	Microphone	Chest	Surrounding sound effects
SCG	Contacted	HR	Mechanical	Accelerometer	Chest	Motion artifacts
PPG	Contacted	HR, RR, BP	Light	Photo-diode	Finger	Motion artifacts
Mercury sphygmomanometer	Contacted	BP	Pressure	Pressure sensor	Upper arm	Noncontinuous measurement
Oscillometry	Contacted	BP	Pressure	Pressure sensor	Upper arm	Noncontinuous measurement
Thermal imaging	Non-contacted	HR, RR	Temperature	Thermal camera	Skin	Motion artifacts
RGB imaging	Non-contacted	HR, RR, BP	Light	RGB camera	Skin	Light effects
Acoustic sensing	Non-contacted	HR, RR	Mechanical	Speakers and microphones	Chest	Motion artifacts
LDV	Non-contacted	HR, RR	Mechanical	Laser sensor	Chest/Neck	High cost
Radar	Non-contacted	HR, RR, BP	Mechanical	Radio sensor	Chest	Motion artifacts

sign monitoring methods, such as camera-based techniques, acoustic sensing, **laser Doppler vibrometer (LDV)**, and radar-based methods, are widely investigated. In Table 2, we present a comprehensive comparison of these non-intrusive measurement methods alongside conventional contact-based measurement techniques.

Camera-based methods for monitoring vital signs can be divided into thermal imaging and RGB imaging based on the different ways of observing physiological phenomena. Thermal cameras monitor cardiac and respiratory activity by sensing minute heat changes caused by pulsating blood flow in major superficial arteries and respiration near the nostrils [32, 33]. RGB cameras monitor subtle skin color variations due to inconsistent blood volume in arteries and capillaries [34, 35]. Signals detected by an RGB camera can be considered a type of remote PPG signal.

Due to the privacy issues caused by using cameras, researchers have also explored methods based on acoustic sensing. It leverages the speakers of smart devices to emit continuous frequency-modulated ultrasonic signals that are not perceived by human ears. These signals are modulated by the surface motion of the human body caused by vital activities and captured by microphones [36, 37]. However, this acoustic signal-based method has certain limitations. The sensing range is restricted by the transmission power of the smart device, and it requires more advanced signal processing methods to extract vital signs.

LDV-based vital sign monitoring is a promising long-range contactless technology [38], using a low-power laser to detect vibrations caused by cardiovascular activities on skin surfaces and extract cardiac events from the reflected signals. Another long-range vital sign sensing method is based on microwaves (300 MHz–300 GHz). According to the wavelength, it can be categorized into decimeter-wave, centimeter-wave, and mmWave (the focus of our survey). Decimeter waves, with their comparatively large wavelengths, inherently prove unsuitable for capturing centimeter-level vital activities, rendering the analysis of acquired signals a formidable challenge. Centimeter waves sense vital activities with limited accuracy, while mmWaves have a shorter wavelength and are more sensitive to millimeter-level displacement. Johnson and colleagues [39] utilized an FMCW radar operating at 57–63 GHz to capture the millimeter-scale motion of the artery and reconstruct the arterial pulse waveform. As demonstrated in Figure 3, the reconstructed signal shows a strong correlation with the results obtained through tonometer detection.

### 3 MMWAVE RADAR

#### 3.1 mmWave Brief History

Millimeter waves (mmWave) are electromagnetic waves with wavelengths between 1 mm and 10 mm, corresponding to the radio spectrum between 30 GHz and 300 GHz. The development of mmWave technology dates back to the 1890s, when Lebedew used a spark gap generator to

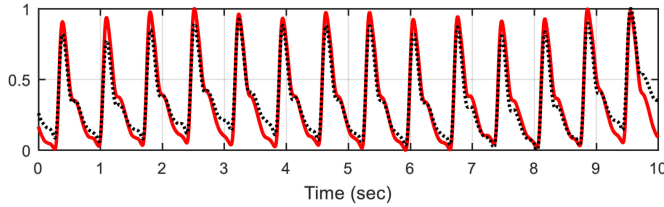


Fig. 3. The radar reconstruction signal (red, solid) and tonometer reference signal (black, dotted) [39].

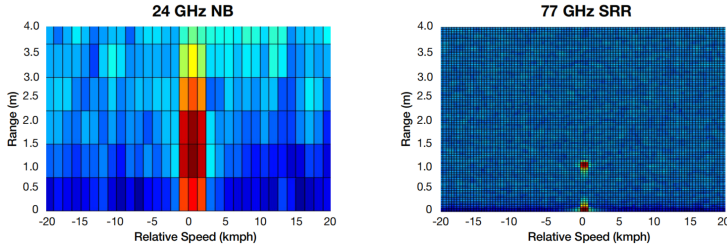


Fig. 4. The Range-Doppler map of detecting stationary objects at a distance of 1 m using 24 GHz (left) and 77 GHz (right). The results show the 77 GHz sensor has 20x better range resolution and 20x better velocity resolution compared to the 24 GHz sensor [40].

generate millimeter waves at 6 mm wavelengths. However, the spark gap generator was not stable and produced incoherent signals. In the 1930s, early types of magnetrons were invented, followed by cavity magnetrons in 1939, which were used in radar systems during World War II.

Post-war, numerous institutions began researching mmWave, leading to the development of high-resolution 70 GHz radars by the U.S. Army Signal Engineering Laboratories, Bell Laboratories, and Georgia Tech in the 1960s. The advent of solid-state sources and new vacuum tube sources in the 1970s further advanced mmWave technology. Breakthroughs in high-power coherent radiation sources, high-stability sources, transmission media, and mmWave components, combined with injection locking and phase locking technologies, significantly improved the resolution and availability of mmWave sensors.

- Smaller antenna: The wavelength of mmWave is millimeter-level, so the antenna size can be small. This reduces the size of the antenna array and improves the integration density of the radar.
- High resolution and precision: Compared to lower band wave, mmWave has higher range resolution, velocity resolution, and angle resolution for the same antenna size. As shown in Figure 4, the 77 GHz sensor has higher velocity resolution and range resolution than the 24 GHz sensor.
- Anti-interference: The mmWave has strong penetrating ability—even in poor weather conditions such as clouds and fog, it still has good detection capability.

### 3.2 Comparison of mmWave Modulation Methods

Owing to the growing demand for various applications of mmWave radar, these radars transmit signals using multiple modulation patterns to cater to different measurement requirements. The modulation of radar signals encompasses pulse modulation and **continuous wave (CW)** modulation, differing in the form of the modulated signal. Pulse and CW modulation are associated with the two primary radar systems: pulse radar and CW radar. Pulse modulation's basic unit is a pulse,

Table 3. Comparison of mmWave Modulation Methods

Feature	Pulse wave	CW	FMCW	SFCW
Range detection	Yes	No	Yes	Yes
Blind range	Yes	No	No	No
Signal leakage	No	Yes	Yes	Yes
Multiple target detection	Yes	No	Yes	Yes
Complexity of system architecture	High	Simple	Medium	Medium

and from the viewpoint of pulse parameters impacted by modulation, it can be divided into **pulse amplitude modulation (PAM)**, **pulse phase modulation (PPM)**, **pulse width modulation (PWM)**, and **pulse code modulation (PCM)**. In vital sign monitoring applications, a rectangular wave modulated by PPM serves as a classic pulse wave. CW modulation, however, is a continuous signal with a stable high frequency. Frequency modulation, a common type of CW modulation used in vital sign monitoring, is known as **frequency-modulated continuous wave (FMCW)** radar. The advantages and disadvantages of unmodulated mmWave (i.e., CW) are presented in Table 3.

Rectangular waves comprise a series of short, repetitive pulses, each with a constant frequency [41]. The target's range can be estimated by the time of flight between the emitted and reflected pulses, while chest motion is measured by amplitude. In pulse-based sensing, the receiving and transmitting processors share a single antenna in a time-division manner. This pulse-based method effectively prevents signal leakage compared to modulation where receiving and transmitting processors operate simultaneously. However, pulse radar results in blind ranges due to time intervals between transmitted pulses, corresponding to the receiver being off for the pulse to reflect from the target, rendering the radar unable to measure the target.

In this article, the unmodulated CW refers to the sine wave. The velocity information carried by the reflected wave is analyzed to detect and track the target based on the Doppler effect principle, and vital signals are obtained by phase-demodulating the human-reflected signal. A notable advantage of CW over pulsed waves is their continuous results. Nevertheless, unmodulated CW can only track relative motion and cannot detect the target's range, making it unsuitable for vital sign detection of multiple targets. Moreover, CW-based sensing is noise-sensitive due to its inability to separate reflections from different locations, thus rendering it inapplicable in multi-object scenarios.

In contrast to CW modulation, FMCW changes the transmitted signal's frequency during measurement, mapping range information to frequency differences to address CW's ranging incapability [42]. FMCW-based sensing can transmit relatively high power via frequency modulation techniques to achieve high SNR and utilize MIMO antennas to track and locate multiple targets. However, the hardware system of FMCW-based sensing is more complex than that of CW-based sensing, necessitating greater power consumption and more advanced signal processing methods. FMCW radar modulation patterns typically include sawtooth, triangular, square-wave, stepped, and sinusoidal waveforms, with the sawtooth wave being the most commonly used modulation for vital sign sensing. Therefore, this article's default FMCW frequency pattern is based on the sawtooth wave.

SFCW [43] is another frequency modulation waveform, consisting of  $N$  equidistant scattering frequencies within a specified bandwidth and used with FMCW radar as stepped frequency modulation patterns. The range resolution of a target is inversely proportional to the bandwidth, and the maximum unambiguous range distance at which targets can be distinguished depends on the number of frequency steps. FMCW can be considered as SFCW with infinitely small frequency steps and an infinitely large number of steps, providing higher resolution.

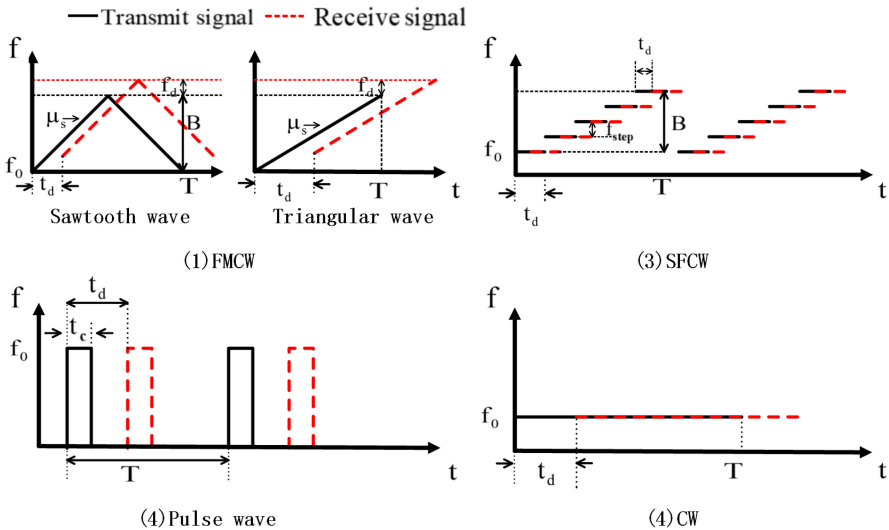


Fig. 5. The Time domain waveforms with different modulation patterns, where  $f_0$  is the starting frequency of the signal,  $\mu_s$  is the slope of the signal,  $T$  is the width of chirp signal pulse,  $B$  is the bandwidth,  $t_d$  the time delay, and  $f_{step}$  is the frequency step.

The fundamental time domain waveforms associated with various modulation patterns are depicted in Figure 5. In specific scenarios, more intricate signal modulation is employed. Each signal waveform possesses unique advantages and characteristics tailored to the particular requirements of the application field. Continuous vital signs induce small, micron-scale vibrations, and real-life detection scenarios are consistently complex, involving multi-object situations or background clutter. FMCW has been demonstrated to be well-suited for vital sign sensing, providing high range and velocity resolution.

### 3.3 Differentiation of RF Sensing Technologies

In addition to mmWave, researchers have also investigated RF-based heart rate sensing technologies based on different frequencies such as Wi-Fi, IR-UWB radar, and **Terahertz (THz)**.

Wi-Fi-based vital signs sensing technology utilizes Wi-Fi radio signals to track human activity, movement, and vital signs. Wi-Fi is more cost-effective compared to mmWave, as almost all medical and residential environments are equipped with Wi-Fi devices. References [44, 45] have demonstrated the extraordinary ability to track vital signs using Wi-Fi signals. However, these works have some limitations such as high dependence on multiple environment-related parameters (e.g., location of Wi-Fi transceiver, line-of-sight/non-line-of-sight conditions) and many challenges in multi-person vital signs monitoring scenarios.

IR-UWB radars (3.1 to 10.6 GHz) utilize very short pulsed signal (on the order of nanoseconds) that occupy greater than 500 MHz or 25% of the frequency band. The nature of this pulsed signal allows IR-UWB radar to achieve centimeter-level target ranging accuracy and strong obstacle penetration [46]. Since it uses very low power to transmit pulses, there is no health risk and it can be used on a daily basis [47]. Compared to mmWave radar, IR-UWB radar has a stronger ability to penetrate obstacles and is more applicable for detecting vital signs in **non-line-of-sight (NLOS)** scenarios (e.g., rescue operations) [48, 49]. However, mmWave radar has a higher range resolution, which can provide finer vital sign bins localization information and performs better in **line-of-sight (LOS)** scenarios. In general, higher frequencies represent better range resolution,

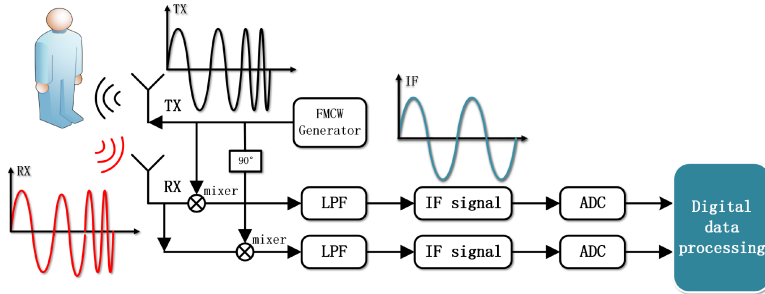


Fig. 6. An FMCW-based system block diagram.

along with weaker penetration capabilities. Low resolution range bins lead to clutter noise, especially in crowded environments/targets. For example, the range resolution at 60 GHz is 1.7 cm, which is sufficient for the detection of breathing motions (a few mm to 1 cm). However, it is challenging to detect micro-movements of the heart (less than 1 mm) with such range resolution that includes breathing motions and other body motions, as well as clutter noise from other scatters (e.g., clothing). These limitations may be alleviated by using higher operating frequencies such as terahertz (THz, 100 GHz–10 THz).

THz offers larger bandwidth, which can increase the range resolution and thus reduce clutter noise. For instance, at 300 GHz, the range resolution can reach 3.3 mm. In addition, THz provides high phase sensitivity. For example, a motion of 0.5 mm causes a phase change of 3.6° at 60 GHz, while at 300 GHz the corresponding phase change is 18°. This feature allows tiny motions related to vital activities, such as chest micro-motions by breathing, heart-caused micro-motions [50], and surface skin motion caused by blood flow [51], to be easily detected by the phase method. THz has significant advantages over mmWave, however, terahertz technology is currently not mature enough for application, and the equipment costs are expensive.

#### 4 MVSS SIGNAL MODEL

The radar system transmits an electromagnetic wave signal that is obstructed and reflected by objects in its path. By analyzing the reflected signal, the radar system can determine the object's distance, speed, and angle. To comprehend how human physiological activity modulates the reflected signal, researchers have developed various mathematical models to characterize the signal for subsequent processing. In this section, we summarize four MVSS signal models. The first model is based on phase modulation resulting from chest vibrations due to human physiological activities, with geometric properties within the phase IQ domain offering a novel perspective. Another model is based on the cardiac electromagnetic field, and the final model is based on the multipath effect.

##### 4.1 The Chest Micro-motion Model

**4.1.1 FMCW-based Sensing.** The principle of FMCW-based remote sensing of vital signs is based on the phase modulation of the **intermediate frequency (IF)** signal by the vital micro-motion of the human body. A simplified block diagram of a typical FMCW-based sensing system is shown in Figure 6. The IF signal is obtained by mixing the transmitted signal and the reflected signal and then filtering out the high-frequency components.

The emitted chirp of An FMCW radar can be expressed as:

$$x_T(t) = A_T \cos \left( 2\pi f_0 t + \pi \frac{B}{T_c} t^2 \right), \quad (1)$$

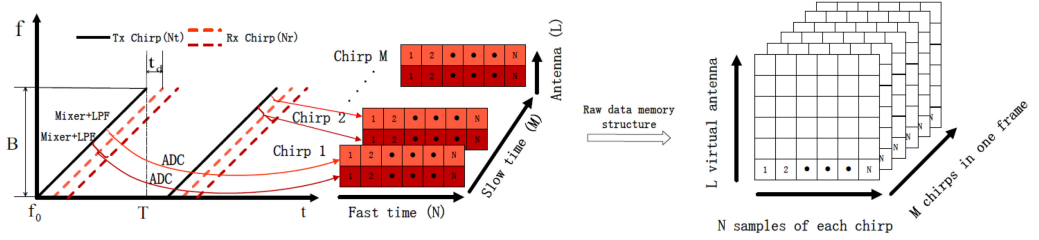


Fig. 7. ADC data cube structure. The sensing system transmits FMCW and the received reflected wave is mixed by a mixer and then passed through an LPF to obtain the IF signal. The raw data is the output of the IF signal sampled by ADC where  $N_t$  is the number of transmitter antennas,  $N_r$  is the number of receiver antennas,  $N$  is the number of samples in a chirp,  $M$  is the number of chirps in a frame and  $L(L = N_t \times N_r)$  is the number of virtual receivers.

where  $A_T$  is the amplitude of the transmitted chirp,  $f_0$  denotes the starting frequency of the transmitted chirp,  $B$  means the bandwidth of the transmitted chirp, and  $T_c$  is the duration of the transmitted chirp. The received signal is the delayed version of the transmitted signal. Assuming the range between a target with a sensing system is  $d$  and the change of chest displacement caused by cardiopulmonary activity with time is expressed as  $x(t)$ . The time delay of the received signal and the received signal, respectively, can be described as:

$$t_d = 2 \frac{d + x(t)}{c}, \quad (2)$$

$$x_R(t) = A_R \cos \left( 2\pi f_0 (t - t_d) + \pi \frac{B}{T} (t - t_d)^2 \right), \quad (3)$$

where  $c$  and  $A_R$  are the speed of radio wave propagation in the air and the amplitude of the received signal, respectively. The received signal and the transmitted signal are mixed by two orthogonal I/Q channels and then passed through a low-pass filter to obtain the IF signal  $x_{IF}(t)$

$$x_{IF}(t) \approx A_T A_R e^{j \left( 2\pi \underbrace{\frac{2Bd}{cT}}_f t + \underbrace{\frac{4\pi(d+x(t))}{\lambda}}_{\psi(t)} \right)}, \quad (4)$$

$$= A_T A_R e^{j(2\pi f t + \psi(t))},$$

where  $f$  is the frequency of the IF signal, which is related to the range between the sensing system and the target,  $\psi(t)$  denotes the phase of the IF signal, which is associated with chest motion when the target remains relatively stationary, and  $\lambda$  is the signal wavelength. Hence, to observe the change in chest displacement, it is necessary to sequentially transmit multiple chirps to obtain the phase change information. Multiple continuous IF signals can be represented in fast time and slow time as the  $n$ th sample point and the  $m$ th chirp:

$$R[m, n] = A_T A_R e^{j(2\pi f n T_f + \frac{4\pi}{\lambda} (d + x(n T_f + m T_s)))}, \quad (5)$$

where  $T_s$  means the time interval of emitting chirp, i.e., the phase sampling interval for the chest motion, and  $T_f$  is the sampling period for a single chirp. Furthermore, when the sensing system has multiple receiving antennas, the discrete ADC data is shown in Figure 7. And when the antenna array is a linear array, the signal model can be rewritten as:

$$R[m, n, l] = A_T A_R e^{j(2\pi f n T_f + \frac{4\pi}{\lambda} (d + x(n T_f + m T_s)) + \frac{2\pi}{\lambda} a_l \sin \theta)}, \quad (6)$$

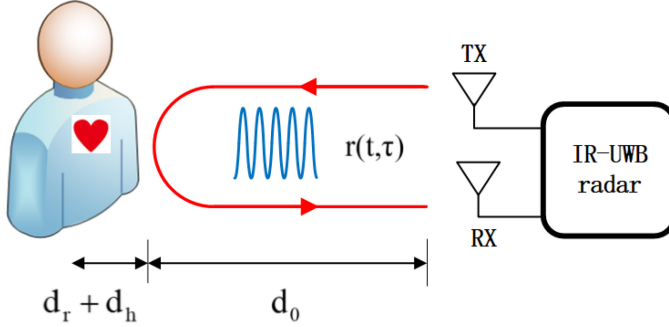


Fig. 8. A schematic diagram of the IR-UWB radar detection principle.

where  $\frac{2\pi}{\lambda}a_l \sin \theta$  represents the phase difference between the reflected signal received by the  $l$ -th antenna from the target located at the arrival of angle  $\theta$  and the reflected signal received by the first antenna.

Assuming there are  $k$  targets in the **field of view (FoV)** of the sensing system and the range-angle information of each target is  $(d_b, \theta_b)$ , the signal model can be extended as a superposition of multiple target reflected signals:

$$R_k[m, n, l] = \sum_{b=1}^k A_T A_R \exp \left( j \left( 2\pi f_b n T_f + \frac{4\pi}{\lambda} d_b + \frac{4\pi}{\lambda} x_b (n T_f + m T_s) + \frac{2\pi}{\lambda} a_l \sin \theta_b \right) \right). \quad (7)$$

In summary, when the position of the target  $(d, \theta)$  is fixed, the relative phase change over slow time  $\theta(mT_s)$  is caused by the chest displacement, which can be described as:

$$\theta(mT_s) = \frac{4\pi x(mT_s)}{\lambda}, \quad (8)$$

where  $\theta(mT_s)$  is the feature for vital signs estimation.

**4.1.2 IR-UWB Radar Sensing.** Vital signs remote sensing using IR-UWB radar is based on the amplitude variations and **time of arrival (ToA)** of the reflected pulses to derive the status of the cardiorespiratory activity.

The principle of IR-UWB radar detection is shown in Figure 8. Assuming the fluctuating motion of the chest caused by respiration and heartbeat are the sinusoidal signals  $d_r$  and  $d_h$ , respectively, the distance between the source of the vital signal and the antenna can be expressed as:

$$d(t) = d_0 + d_r + d_h = d_0 + A_r \sin(2\pi f_r t) + A_h \sin(2\pi f_h t), \quad (9)$$

where  $t$  is the observation time,  $d_0$  is the nominal distance between the antenna and the human chest wall,  $A_r$  denotes the displacement amplitude of respiration,  $A_h$  is the displacement amplitude of the heartbeat, and  $f_r$  and  $f_h$  represent the respiration frequency and the heartbeat frequency, respectively.

Therefore, the time delay of the reflected signal received by the IR-UWB radar from the target can be represented as:

$$\tau_k(t) = \frac{2d(t)}{c} = \tau_0 + \tau_r \sin(2\pi f_r t) + \tau_h \sin(2\pi f_h t), \quad (10)$$

where  $c$  is the propagation speed of the pulse wave,  $\tau_0 = 2d_0/c$ ,  $\tau_r = 2A_r/c$ , and  $\tau_h = 2A_h/c$ . Let  $\delta(t)$  be the normalized received pulse, and the total impulse response can be represented

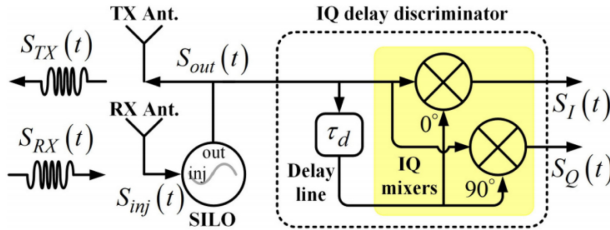


Fig. 9. A block diagram of the self-injection-locked (SIL) radar system [52].

by:

$$r(t, \tau) = A_k \delta(\tau - \tau_k(t)) + \sum_i A_i \delta(\tau - \tau_i), \quad (11)$$

where  $\tau$  is the sampling time of each pulse,  $A_k$  is the response amplitude from the human body, and  $A_i$  and  $\tau_i$  are the response amplitude of each multipath component and the delay of each multipath, respectively. And the reflected signal received by the receiving antenna can be regarded as the convolution of the transmitted pulse signal and the response function, which is expressed by the following equation:

$$R(t, \tau) = s(\tau) * r(t, \tau) = A_k s(\tau - \tau_k(t)) + \sum_i A_i s(\tau - \tau_i), \quad (12)$$

where  $s(t)$  is the first-order Gaussian pulse signal. And the discretized Equation (12) can be written as:

$$\begin{aligned} R[m, n] &= R(mT_s, nT_f) \\ &= A_k s(nT_f - \tau_k(mT_s)) + \sum_i A_i s(nT_f - \tau_i), \end{aligned} \quad (13)$$

where  $m$  and  $n$  are the sampling numbers in slow time and fast time, respectively.  $T_s$  is the pulse repetition interval in slow time, and  $T_f$  is the fast time sampling interval.

**4.1.3 SIL-based Sensing.** The SIL-based sensing system employs a unique **SIL oscillator (SILO)** that relies on the principle of injection locking as its signal source. It injects the received signal into the SILO, putting it into an injection-locked state. Injection locking occurs when an oscillator is interfered with by a second oscillator with a sufficiently close frequency, resulting in the capture of the first oscillator, which then essentially shares the same frequency as the second oscillator. Figure 9 illustrates the fundamental structure of the SIL radar system. In a SIL radar, the SIL oscillator generates the radar transmission signal ( $S_{TX}(t)$ ), while the radar reception signal ( $S_{RX}(t)$ ) is input as an injection signal ( $S_{inj}(t)$ ) to the SILO, inducing the SIL state. The output signal from the SILO then passes through the IQ delay discriminator, producing the IQ signal.

Assuming the SILO possesses an inherent oscillation frequency  $\omega_{osc}$ , a constant oscillation amplitude  $E_{osc}$ , and a tank quality factor  $Q_{tank}$ . When a reflected signal with an instantaneous frequency  $\omega_{inj}(t)$  and a constant amplitude  $E_{inj}$  is introduced into the SILO, the instantaneous output frequency of the SILO,  $\omega_{out}(t)$ , can be represented as follows:

$$\omega_{out}(t) = \omega_{osc} - \omega_{LR} \sin \alpha(t), \quad (14)$$

where  $\omega_{LR}$  is the locking range and  $\alpha(t)$  means the instantaneous phase difference between the injection signal and the oscillation signal.  $\omega_{LR}$  and  $\alpha(t)$  is given by

$$\omega_{LR} = \frac{\omega_{osc}}{2Q_{tank}} \frac{E_{inj}}{E_{osc}}, \quad (15)$$

$$\alpha(t) = \frac{\omega_{osc}}{c} (2R + 2x(t)), \quad (16)$$

where  $R$  and  $x(t)$  represent the distance to the target and the instantaneous displacement of the target, respectively, while  $c$  denotes the speed of light. By substituting Equations (15) and (16) into Equation (14), the frequency-demodulated output signal,  $S_{bb}(t)$ , can be approximated as follows:

$$\begin{aligned} S_{bb}(t) &= \arctan \left( \frac{-S_Q(t)}{S_I(t)} \right) \\ &\approx \pi \cdot \text{Mod}(\omega_{osc}\tau_d, \pi) - \omega_{LR}\tau_d \sin \left( \frac{2\omega_{osc}R}{c} \right), \\ &\quad - \frac{\omega_{osc}^2 \tau_d}{Q_{tank}c E_{osc}} \cos \left( \frac{2\omega_{osc}R}{c} \right) \cdot x(t), \end{aligned} \quad (17)$$

where Mod denotes a modulus function and  $\tau_d$  is the delay time of the delay unit in the frequency demodulator. The first and second terms on the right side determine the **direct current (DC)** offset of the signal and can be removed by adjusting  $\omega_{osc}$ . If the clutter is stationary ( $x(t) = 0$ ), it will result in only a small constant frequency offset in the oscillator output signal of the SIL radar, as opposed to causing a significant DC offset in the baseband signal of a conventional CW radar. Therefore, SIL-based sensing greatly enhances the SNR of the output signal ( $S_{bb}(t)$ ).

In vital sign detection, the detection target is the human body. When the human body position ( $R$ ) is fixed,  $x(t)$  is considered as the chest micro-movement caused by HR and RR, and the vital sign-related signals can be parsed from  $S_{bb}(t)$ .

**4.1.4 SFCW-based Sensing.** The SFCW-based sensing theory is roughly similar to the FMCW-based, with the major differences being in the signal generator and the signal processing. The SFCW signal can be represented as [43]:

$$\begin{aligned} x_T(t) &= \sum_{m=0}^M A_T \cos(2\pi(f_0 + m\Delta f)t), \\ &\quad \cdot \text{rect}\left(\frac{t - mT}{T}\right), \end{aligned} \quad (18)$$

where  $A_T$  is the amplitude of the transmitted signal,  $f_0$  is the starting carrier frequency,  $\Delta f$  means the frequency increment,  $T$  represents the duration time of each frequency, and  $M$  is the number of all carrier frequencies. Thus, the bandwidth of SFCW is  $M * \Delta f$ . To decrease pulse-repetition time, the duration time of single-frequency  $T$  is generally limited to the microsecond level. Besides, the rectangle function is given by

$$\text{rect}\left(\frac{t}{T}\right) = \begin{cases} 1, t \in (-T/2, T/2) \\ 0, \text{otherwise} \end{cases}. \quad (19)$$

The radar received signal is the time delay of the transmitted signal, which can be expressed as:

$$\begin{aligned} x_R(t) &= x_T(t - t_d) \\ &= \sum_{m=0}^M A_R \cos(2\pi(f_0 + m\Delta f)(t - t_d)) \\ &\quad \cdot \text{rect}\left(\frac{t - t_d - mT}{T}\right), \end{aligned} \quad (20)$$

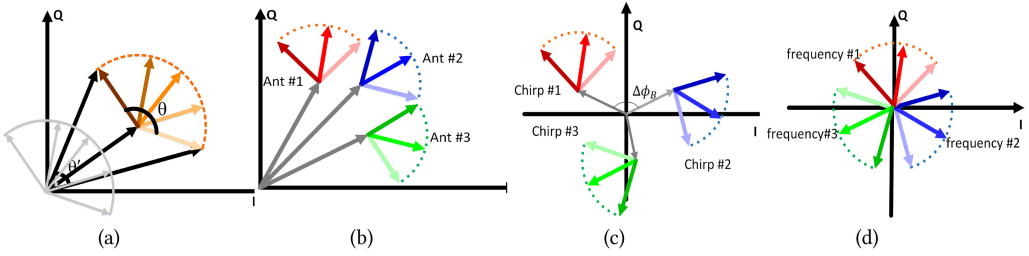


Fig. 10. Geometric properties in the IQ domains: (a) Ideal/Practical chirp signals; (b) Practical multi-antenna signals; (c) Practical multi-chirp signals; (d) Ideal multi-frequency signals.

where  $t_d = \frac{2R(t)}{c}$ . After the mixer and LPF, the system output signal is as follows:

$$x_{IF}(t) = \sum_{m=0}^M A_T A_R \cos \left( \frac{4\pi f_0 R(t)}{c} + \frac{4\pi m \Delta f R(t)}{c} \right) \cdot \text{rect} \left( \frac{t - t_d - mT}{T} \right). \quad (21)$$

Through ADC sampling in each frequency in Equation (21), a period of multi-frequency echo data is obtained as a frequency-domain complex data vector. Assume  $N$  periods of SFCW echoes are collected. Therefore,  $N$  periods of data vector can be combined into a  $M \cdot N$  dimensions of data matrix  $S$ , where the element of  $n$ th row (period) and  $m$ th column (frequency) can be expressed as:

$$S(n, m) = \sum_{m=0}^M A_T A_R \cos \left( \frac{4\pi f_0 R(n)}{c} + \frac{4\pi m \Delta f R(n)}{c} \right). \quad (22)$$

where  $4\pi f_0 R(n)/c$  indicates the phase change due to the chest fretting of the target, which can be analyzed to estimate vital signs.

## 4.2 Geometric Properties in IQ Domains

The phase change of the reflected signal from the target is connected to the target's minor fluctuations in displacement and velocity when using FMCW-based sensing or CW-based sensing. However, noise can inevitably impact the accuracy of phase extraction, particularly the phase distortion caused by DC offset. Examining the geometric properties of the phase signal in the IQ domain, with a focus on DC offset, is also a promising approach for reliably extracting phase changes.

The vibration phase signal in the IQ domain is theoretically a circular arc centered at the origin of the coordinates. In reality, the center of the circular arc is irregularly shifted away from the coordinate origin, a phenomenon known as DC offset. As illustrated in Figure 10(a), the extracted phase changes differ in the two cases. Since the extracted phase ( $\theta'$ ) deviates from the true phase ( $\theta$ ), the circle fitting method is employed in References [53–55] to eliminate DC offset by dynamically tracking the position of the circle's center and moving it to the coordinate origin. However, the circle fitting method may yield unstable fitting results and inaccurate vibration measurements for small arcs. The phase signal generated by tiny vibrations is a small arc in the IQ domain, and simple circle fitting is insufficient for handling these vibrations. A more comprehensive analysis of the geometric properties of the phase signal in the IQ domain is needed. The phase signal of the same antenna at different moments or different antennas at the same moment will exhibit varying DC offsets, as shown in Figures 10(b) and 10(c). Increasing the number of observations for the same moment of vibration can help form a larger arc, thereby reducing measurement error.

According to Equation (4), the phase  $\psi(t)$  can be expressed as:

$$\psi(t) = 4\pi \frac{d + x(t)}{\lambda} = 4\pi f_0 \frac{d + x(t)}{c}. \quad (23)$$

Equation (23) demonstrates that  $\psi(t)$  is dependent on  $f_0$  and  $x(t)$  when the target is stationary (with a fixed  $d$ ). While  $x(t)$  is beyond our control, the starting frequency ( $f_0$ ) of the chirp can be adjusted in the sensor. By altering  $f_0$  and maintaining the same  $x(t)$ , ideally, the phase signal in the IQ domain will rotate around the coordinate origin, as depicted in Figure 10(d). If we establish a set of chirps with varying  $f_0$  for simultaneous measurement, then the phase information will form a larger arc in the IQ domain. This larger arc is beneficial for fitting a more accurate circle.

### 4.3 The EM Field Model

The detection of vital signs can be based on physical phenomena associated with the **electromagnetic (EM)** field, such as the dielectric properties (permittivity) of biological matter and the Faraday effect. The permittivity of biological materials (e.g., blood, cellular tissue) changes in response to an external EM field, with unique changes for different materials. The presence of an electric field allows biomaterials with electrical conductivity to detect permittivity, enabling the conversion of biological responses into measurable signals. In summary, biosensors made from biomaterials are utilized to detect permittivity changes to analyze the composition of biological materials, such as identifying cancer cells in tissues or measuring blood glucose concentrations. Although most biosensors require contact, non-contact detection based on permittivity is challenging. However, the Faraday effect offers a new approach for non-contact detection. According to this effect, a polarized high-frequency EM wave (mmWave) is rotated by the cardiac EM field during scattering in the chest, allowing for the inference of cardiac activity by analyzing the reflected signal.

**4.3.1 EM Field Description.** Dielectric exhibits conductive properties under an externally applied electric field. In the EM field, the positive charge in the dielectric gets displaced in the direction of the electric field and the negative charge is displaced in the opposite direction. The conduction of charge in a dielectric produces conduction currents, while the displacement of charge due to polarization produces displacement currents. Polarization and conduction currents result in the loss of EM energy in the dielectric [56], which can be described as:

$$\epsilon^* = \epsilon' - j\epsilon'', \quad (24)$$

where  $\epsilon'$  is the real part of permittivity and  $\epsilon''$  is the loss factor caused by conduction and polarization losses. The complex form of the permittivity can better explain the EM energy loss in the dielectric, where the imaginary part is called the loss factor.

In an alternating magnetic field, charges attempt to align themselves with the applied field's direction, and the time required for the charges to catch up with the changing field is called the relaxation time. As the frequency increases, the time for charges to align becomes shorter, eventually reaching a point where they can no longer keep up. This frequency is known as the relaxation frequency. Debye's equation provides a model for how permittivity varies with frequency. At low frequencies, the dipole has sufficient time to follow the changing applied field. As frequency increases, the dipole cannot fully recover its original position, resulting in a loss of permittivity. When the applied frequency aligns with the relaxation frequency, polarization can no longer keep up with the rapidly changing electric field and disappears, causing a drop in permittivity.

The permittivity spectrum offers a unique dielectric property that can be used to analyze biological targets within biological matter. These targets can be biomolecules such as proteins, DNA, biomarkers, pathogenic organisms, hormones, or other medically relevant analytes such as glucose,

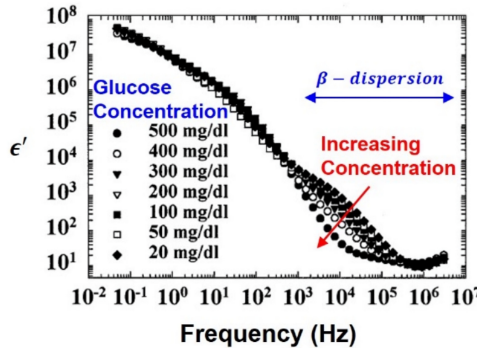


Fig. 11. Permittivity spectrum of glucose concentration [57]. Differential permittivity can be observed for different concentrations of blood glucose at EM fields from 1 KHz to 100 KHz.

pulse, and heartbeat. Biosensors measure cells and tissues' unique permittivity curves directly or indirectly, allowing for the identification of these biological targets. For example, in a glucose biosensor, glucose concentration changes on the detection surface result in permittivity changes and shifts in relaxation frequency, as shown in Figure 11. In another case, tumor cell assays exploit the difference in cytoplasmic content between dead or tumor cells and live, healthy cells, providing a permittivity contrast.

**4.3.2 Cardiac EM Field.** Modern medicine indicates the presence of electrical activity in the human body; this electrical activity is generated by cells. By controlling the flow of charged elements (e.g., potassium ions and sodium ions) across the cell membrane, the cell creates a potential difference between the inside and outside of the cell to generate electrical currents, which can be turned into an electrical impulse called an action potential. The human body uses certain patterns of action potentials to perform physical actions, thoughts, and behaviors. And each mechanical heartbeat is triggered by action potentials originating from the pacemaker cells (sinoatrial node) within the heart. The impulse is then conducted rapidly throughout the organ to produce a coordinated contraction. In contact detection, clinical ECG systems measure the electric current on the surface of the body through electrode patches to help diagnose cardiac disease. In non-contact detection, the Faraday effect [58] provides the idea of remotely sensing the changes in the cardiac EM field. Specifically, polarized high-frequency EM waves (i.e., mmWave) can be rotated by modulation of the cardiac EM field extending outside the body during scattering to the chest surface, which will change the frequency of the received signal. The periodically varying cardiac EM field generated by the electrical activity of the heart periodically modulates the sequentially transmitted mmWave signal. Xu et al. [59] proposed the CardiacWave, which used mmWave radar to capture the periodic changes in the Cardiac EM field and provide a full spectrum of ECG-like heart activities, including the details of P-wave, T-wave, and QRS complex. The mmWave scattering at the chest surface will be impacted by a path-dependent mismatch factor  $\beta_L(t)$ , which can be expressed as:

$$\beta_L(t) = \int_V \cos^2(\nu\mu H(t, r)dl), \quad (25)$$

where  $\nu$  is the Verdet constant,  $\mu$  is the permeability,  $L$  represents the mmWave propagating path, and  $H(t, r)$  represents distributed about the location and time. Eventually, The modulation of the mmWave by the cardiac EM field can be expressed as:

$$C(t) = \sum_L A_t \exp j[2\pi f_t] \beta_L(t), \quad (26)$$

where  $A_t$  and  $f_t$  represent the amplitude and frequency of the mmWave, respectively. Equation (26) shows the scattered mmWave response at different frequency components has frequency shift associated with the cardiac EM field.

#### 4.4 Based on Multipath Effects

During WiFi communication, the wireless signal that is received can be understood as a combination of signals that pass through both the direct path and the reflected path of multiple objects. By extracting the physical layer properties of the wireless channel, it can help us understand the change in the environment. In the research area of using WiFi to detect vital signs, the used physical layer information is changing from **received signal strength indicator (RSSI)** to **channel state information (CSI)**. Compared to RSSI, which can only provide an overall description of the received signal, CSI can provide fine-grained channel states information such as amplitude and phase. The channel can be regarded as each subcarrier between the transmit and receive antenna pairs in the WiFi system using **orthogonal frequency division multiplexing (OFDM)** modulation and MIMO techniques. For each subcarrier, the WiFi channel is expressed as:

$$Y_i = H_i X_i + N_i, \quad (27)$$

where  $Y_i \in R^n$  and  $X_i \in R^m$  represent the  $i$ th received and transmitted subcarrier signal, respectively, with  $m$  transmitting antennas,  $n$  receiving antennas.  $H_i$  and  $N_i$  are CSI matrix of  $i$ th subcarrier and noise component, respectively. And  $H_i$  can be represented as:

$$H_i = \begin{pmatrix} h_i^{1,1} & h_i^{1,2} & \dots & h_i^{1,n} \\ h_i^{2,1} & h_i^{2,2} & \dots & h_i^{2,n} \\ \vdots & \vdots & \ddots & \vdots \\ h_i^{m,1} & h_i^{m,2} & \dots & h_i^{m,n} \end{pmatrix}, \quad (28)$$

where  $h_i^{j,k}$  is the CSI of  $i$ th subcarrier between the  $j$ th transmitting antenna and the  $k$ th receiving antenna. Assuming the frequency of the  $i$ th subcarrier is  $f$ , then mathematically  $h_i^{j,k}$  can be expressed as:

$$h(f, t) = e^{-j2\pi\Delta f t} \left( h_s(f, t) + a(f, t) e^{-j2\pi \frac{d(t)}{\lambda}} \right), \quad (29)$$

where  $h_s(f, t)$  is the component from static paths,  $e^{-j2\pi\Delta f t}$  is the phase random offset,  $a(f, t)$ ,  $d(t)$  and  $e^{-j2\pi \frac{d(t)}{\lambda}}$  are path-related complex attenuation, dynamic path length changes due to small body movements and phase shift, respectively.

In summary, CSI contains information about how tiny human motion modulates wireless signals in the time, frequency, and spatial domains. By extracting relevant features such as CSI phase, amplitude, and signal strength, it can help us estimate the vital signs of human targets.

## 5 SIGNAL PROCESSING CHAIN FOR MVSS

Whether based on the chest vibration or on the cardiac EM field, the vital signals contained in the received wireless signal are extremely weak. So, the extraction of vital signals from the received wireless signals is an open problem with many technical challenges, such as motion artifact, random body motion, DC offset, and separation of vital signals. In this section, we summarize a generic signal processing chain for MVSS from a wide range of literature. As shown in Figure 12, we abstract it into four parts: data collection, pre-processing, feature extraction, and vital sign estimation. Specifically, the received signal is first sampled and reconstructed into a format suitable for the next processing step. To focus on the reflection component from the human body, pre-processed is necessary, which includes removing non-human reflections, locating the human body, and so

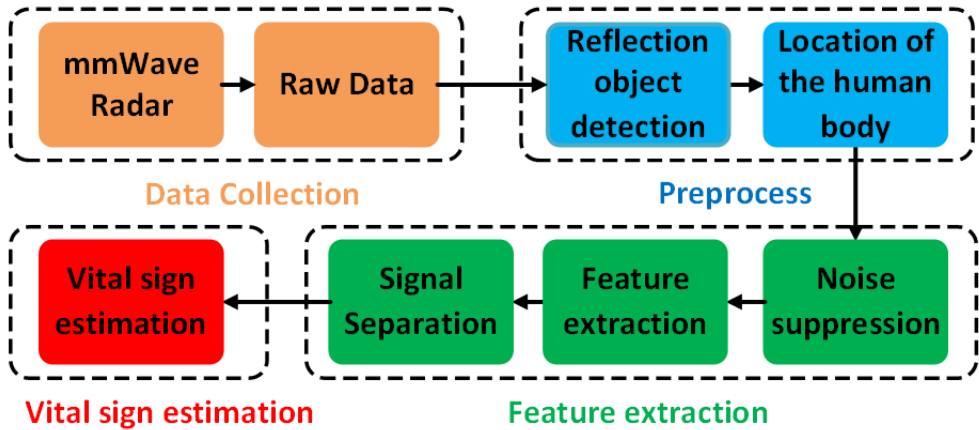


Fig. 12. Signal processing chain for MVSS.

on. Next, the mixed vital signals are extracted from the pre-processed data, compensated, and separated based on the characteristics of different physiological activities. Finally, vital signs are estimated from separated vital signals.

### 5.1 Data Collection and Pre-processing

The wireless signals are sequentially emitted and reflected by objects in the environment (e.g., human body, table, and wall). The reflected signals are received by the receiving antenna and sampled. To simplify the subsequent data processing, the sampled data is usually stored in the form of a data cube (as shown in Figure 7) of the FMCW radar. In the pre-processing stage, the essential task is to search for the reflected object, and the positions of all reflected objects need to be analyzed to determine the human body.

**5.1.1 Reflection Object Detection.** Before locating the human body, we need to parse out all the reflected objects from the data cube to target the potential human object. The position information consists of range and angle. In the case that the human body is far enough away from other objects in the environment, it is possible to localize the human body using only range information. But the angle information is necessary when multiple objects are in close proximity. In addition, separating the body by two dimensions, distance and angle, is beneficial for locating the chest and reducing interference from other parts of the body (e.g., the head and shoulders).

Range information can be acquired by RangeFFT for FMCW [18, 54], which is applied along the sample axis (the fast time axis) to produce the so-called RangeFFT spectra. For SFCW, the typical processing method forms a time-domain range profile with target range information by IFFT pulse compression for each period of a multi-frequency data vector [60].

Target angle information can be resolved from a multi-antenna system. AngleFFT [42] is one of the widely used angle estimation algorithms, which is applied along the antenna axis to obtain the AngleFFT spectra. In addition, digital beamforming can also estimate the **direction of arrival (DOA)**. According to whether the beamformer weights are changed or not, the DOA estimation algorithm can be divided into two categories: fixed beamformer and adaptive beamformer. The classic example of a fixed beamformer is the DOA estimation algorithm introduced by Bartlett in 1965, often referred to as the Bartlett beamformer. However, the Bartlett beamformer can not distinguish two sources whose spatial distance is less than the beam width. The higher-resolution Capon beamformer [61] was proposed in 1969, which is the first proposed adaptive

DOA estimation algorithm and calculates the optimal weights by optimizing the **minimum variance distortionless response (MVDR)** criterion. Capon beamformer requires the inverse of the autocorrelation matrix of the received array data, which introduces high-complexity computations. In 1972, Frost et al. [62] proposed the **linearly constrained minimum variance (LCMV)** beamformer. LCMV beamformer is actually an extended form of MVDR beamformer. In 1979, Schmidt proposed the **multiple signal classification (MUSIC)** beamformer [63], and subsequent researchers have proposed various improved MUSIC algorithms. All of them require eigenvalue decomposition operations to obtain high-precision parameter estimates, which require large computations. In 1985, Roy et al. [64] proposed the **estimation of signal parameters via rotational invariance techniques (ESPRIT)** algorithm, which used some properties of the array signal to solve the function directly and reduce the computational effort. Then, various improved algorithms based on MUSIC and ESPRIT were proposed, such as the minimum parametric method [65], ROOT-MUSIC [66], and TLS-ESPRIT [67]. To avoid the computational complexity of the adaptive beamforming algorithm and improve the effect of DOA estimation, Ahmad et al. [68] combined AngleFFT with Bartlett beamformer. Specifically, the angle information obtained by AngleFFT is used to calculate the optimal weights for the Bartlett beamformer, the optimal weights are recalculated at regular intervals (e.g., every 30 seconds), and the intervals can be set by the user.

The single antenna system can estimate the angle by a dual-station setup [69]. It estimates the target's angle by the range correlation of two single antenna sensing systems. This approach is not recommended if only to obtain angle information. However, multi-station data fusion is a research interest worth exploring and has huge potential for improving detection accuracy and SNR.

**5.1.2 Location of the Human Body.** The reflection signal from the human body will be modulated due to physiological activity, while the reflection signal from the static object is relatively stable. Based on the above fact, the authors of References [4, 55, 70] used a static background elimination technique to distinguish the human body from static objects. Specifically, this technique entailed calculating the mean value of the data in the slow time dimension to establish a baseline background signal, which is subsequently subtracted from the original signal. A more intuitive way to remove stationary objects is based on velocity. From the RangeFFT matrix, Mercuri et al. [18] applied FFT along the chirp axis (the slow time axis) to obtain DopplerFFT spectra for measuring the object velocity. And they filtered static objects by point-by-point multiplication of the RangeFFT matrix and RangeFFT-DopplerFFT matrix. Walterscheid et al. [71] used a **bandpass filter (BPF)** to filter stationary objects, which can be considered as retaining targets within a certain range of velocities.

Motion artifacts occur with the subject's movements is a challenge, which not only decreases the target localization accuracy, but may also produce false targets. In Reference [55], a **constant false alarm rate (CFAR)** detector is used to remove effectively motion artifacts and highlight the moving subject. CFAR is very useful in locating targets. In Reference [72], Acar et al. considered closer targets to cause more powerful returns, CFAR was used to adaptively evaluate the noise level and avoid missing targets away from the radar. ViMo et al. [73] used 1D-CFAR and 2D-CFAR detectors in the range and angle (elevation and azimuth) dimensions, respectively, to estimate the noise level in 3D space, thus providing adaptive thresholds for detecting targets. However, the detection performance of CFAR is correlated with the detection window size and scaling factor. The small detection window is not effective in evaluating the average noise level, while missed detections may occur when using a large window.

Considering the detected target may not be human and the human body will occupy multiple range-angle bins. Therefore, it is important to further identify the locations that contain the vital sign components. Wang et al. [74] located the human major vital bin by checking the variance of the phase information in slow time, the bins corresponding to a human subject are those whose

phase variation over time exceeds a threshold. In Reference [53], the phase is demodulated on all candidate range bins, and the range-vibration map is generated by applying FFT on the slow-time samples. The range bin with the maximum average power is considered as the best choice. To accurately find the human heart location, Ha et al. [75] estimated the HR using a template matching algorithm and then calculated the heartbeat power and total power ratio across coordinates, where the location with the highest power ratio is the heart location. In Reference [73], the presence of the vital signal component was determined by examining the **autocorrelation function (ACF)** of the phase of CSI measurements. This method has a high real-time performance with a small observation window. Based on the fact that the human body has a different permittivity than other objects, the algorithm proposed by Yang et al. [76] evaluated the reflection loss of emerging reflections in an indoor environment to identify whether the reflections are from humans.

## 5.2 Feature Extraction of Vital Signs

As described in Section 4, small-scale physiological activities of the human body modulate the wireless signals. By extracting highly correlated features from the modulated signals, vital signs can be effectively estimated. However, due to the non-ideal hardware and random human motion, the features are often interfered by interference factors that have a great influence on the estimation accuracy. In addition, the extracted features may contain multiple vital signs components (e.g., respiration, heartbeat). Therefore, noise suppression and signal separation are necessary for the measurement performance of vital signs.

**5.2.1 Noise Suppression.** To address the challenge of random body motion, the authors of References [77, 78] attempted to make use of multiple radars placed in different directions to collect the subject information from multiple views. In Reference [79], the information provided by the camera is used to compensate for the phase distortion caused by random body motion. The above multi-sensor approach to cope with random human motion has the same drawbacks of increasing the complexity, cost, and power consumption of the system. Yang et al. [80] proposed a scheme combining adaptive noise cancellation with polynomial fitting, which uses only one Doppler radar to retrieve the components of both respiration and heartbeat signals under random body motion interference. Wang et al. [4] designed a two-step motion compensation algorithm for the in-vehicle environment, which recovers the vital signals from phase information containing driving actions. First, the human targets are aligned by calculating 2-dimensional cross-correlation to compensate large body motion. Second, the B-spline curve is used to estimate motion artifacts to reconstruct vital signals.

As for DC offset, there are two general sources of DC offset. On the one hand, the scattering of stationary clutter (i.e., reflected objects around the target) may result in DC offset. On the other hand, circuit imperfections and direct coupling between the transmitter and receiver may cause DC offset in the RF front-end output.

The DC offset can be compensated by hardware improvements or by back-end data processing. Zhao et al. [81] used a high RF-LO isolation mixer to employ DC coupling. This is complex to implement and was not able to eliminate DC offsets completely. In Reference [82], a radar sensor with DC-coupled adaptive tuning architecture was designed to eliminate most of the DC offset and allowed high gain amplification. Using additional designed hardware to eliminate DC offset from the raw signal requires sufficient expertise, so eliminating DC offset in the back-end data processing is common. As shown in Figure 10(a), the shape of the IQ signal is circular or elliptical, and the center of the circle is offset from the origin. In this situation, calculating the offset circle center is necessary to avoid the phase distortion caused by direct demodulation of the phase. The circle fitting algorithm [53–55] and the ellipse fitting algorithm [83] are commonly used algorithms to correct DC offset. In Reference [76], a BPF with a cutoff frequency of 0.1–20 Hz is applied to the

time-series RSSI signal to remove the DC component and the high-frequency component due to body shaking.

To overcome the amplitude noise and time-varying phase offsets in CSI data, the authors of Reference [84] proposed to use CSI phase difference data between two antennas of the receiver to monitor breathing and heartbeats. Experiments showed that CSI phase difference is more stable and periodic than RSSI in representing vital signs. With a similar aim, References [85] and [86] proposed conjugate multiplication and CSI ratio to resolve time-varying CSI phase shifts and remove amplitude noise, respectively, and to estimate vital signs using both the magnitude and phase of CSI.

**5.2.2 Feature Extraction.** Arctangent demodulation [53, 55], linear demodulation [18, 87], and the **differentiate and cross-multiply (DPCM)** [54] algorithm are widely applied to extract the phase from the IQ domain.

Arctangent demodulation is a classic and simple phase-shift demodulation method that compresses the true phase to  $[-\frac{\pi}{2}, \frac{\pi}{2}]$ , which results in the extracted phase may show phase discontinuities caused by phase jump. For example, if the true phase is  $\frac{3}{4}\pi$ , and the extracted phase using arctangent demodulation turns to  $-\frac{\pi}{4}$ , then it will result in the extracted phase having phase discontinuities caused by phase jump. So, it is necessary to explore the phase unwarping algorithm to improve the phase discontinuity. However, the residual noise makes it difficult to identify these points. To get over the drawbacks of arctangent demodulation, the linear demodulation method based on signal subspace is proposed, which can suppress redundant information and maximize the variance of quadrature data. Massagram et al. [88] suggested the linear demodulation may be a better choice if the signal falls into one of these three categories: (1) relatively short arc lengths produced by the phase transition; (2) low SNR; (3) alternate current coupling is used. But when the phase change is too large, linear demodulation tends to cause distortion. The DPCM algorithm solves the phase jump problem by using differentiation and cross multiplication instead of arctangent and improves the stability of the phase demodulation process.

**5.2.3 Signal Separation.** In general, the extracted phase signal may contain multiple physiological activity information. A typical example is detecting vital signs based on chest micro-motion; the extracted phase signal contains the respiratory and heartbeat components. The amplitude of respiratory vibrations is much greater than that of the heartbeat (about 10 times), and the frequency of respiratory harmonics is close to the heartbeat frequency, so the heartbeat signal is easily covered by the respiratory signal. In addition, the entanglement between breathing and heartbeat signals seriously influences detection accuracy. To overcome the above challenges, scholars proposed their useful schemes for a different scene, e.g., BPF, double parameter **least mean square (LMS)** filter, **wavelet transform (WT)**, **compressive sensing based on orthogonal matching pursuit (CS-OMP)**, **Empirical Mode Decomposition (EMD)**, **Variational Mode Decomposition (VMD)**, and **State space method (SSM)**.

Heart rate and respiratory rate are distributed in different frequency bands. The adult heart rate is about 60–100 beats per minute, and the respiratory rate is 12–20 beats per minute. Designing BPF with different frequencies for heart rate and respiration rate can separate the heartbeat and respiration signals [54, 55, 68, 70, 89–91]. Liu et al. [70] designed the BPF at 0.6–4.2 Hz and 0.1–0.9 Hz to separate heartbeat and respiratory signal, respectively. The BPF-filtered signal may contain residual harmonics and noise. Therefore, the second-order differential filter was employed to highlight the heart signal with an obvious acceleration and to attenuate the respiratory signal in References [92, 93]. He et al. [94] used a double-parameter LMS filter to suppress respiration harmonics and interference. In Reference [54], the CS-OMP algorithm was used to suppress harmonic interference and noise to reconstruct the heartbeat and respiratory signals.

WT, proposed in the 1990s, has the feature of multi-resolution, and the local features of the signal in the time and frequency domains can be represented by the mother wavelet by choosing the appropriate scale and stretch coefficients. Choosing the suitable mother wavelet is crucial to the effectiveness of WT. Mercuri et al. [18, 87], chose the discrete Meyer mother wavelet to separate the heartbeat and respiration signals. In Reference [54], db5 wavelet is selected to perform wavelet decomposition. Wavelet transform has been developed over a long period of time with many improved algorithms, such as **empirical wavelet transform (EWT)** [95] and **stationary wavelet transform (SWT)** [96]. SWT is a wavelet transform algorithm designed to overcome the lack of translation-invariance of the discrete wavelet transform and is used in Reference [97] to separate respiratory signals. EWT integrates the adaptive decomposition concept of EMD and the wavelet transform theory and provides a new adaptive time-frequency analysis idea for signal processing. Compared with the EMD, the EWT is able to select the frequency band adaptively and overcome the modal aliasing problem caused by the signal discontinuity on the time-frequency scale. He et al. [98] presented a study for automated separation of RR and HR signals based on EWT for multiple people.

EMD [99] can be used to separate signals based on a compromise evaluation of the time and frequency and has shown the potential to separate respiratory and heartbeat [100]. However, EMD suffers from mode-mixing and endpoint-effect problems, which restrict its application in practice. To solve this problem, **Ensemble Empirical Mode Decomposition (EEDM)** [101] and **Complete Ensemble Empirical Mode Decomposition with Adaptive Noise (CEEMDAN)** [102] were proposed and applied in References [71] and [103] to separate heartbeat and respiratory signals. Considering respiratory and heartbeat components occur in adjacent components, **principal component analysis (PCA)** and SSM are applied to reconstruct these components in References [104] and [105], respectively. Dragomiretskiy et al. [106] proposed VMD, which is more robust to noise interference compared to the pattern decomposition model. In References [4, 74, 107], VMD is used to separate respiratory or heartbeat signals.

### 5.3 Vital Signs Estimation

After obtaining the relatively clean feature sequence, the next step is to estimate the vital signs based on the feature series to further evaluation of human health status.

**5.3.1 HR/RR Estimation.** HR and RR estimation is usually based on time domain and frequency domain information.

From the time domain, HR and RR are considered as the peak number of the feature sequence within the observation window. In Reference [108], a signal peak-seeking algorithm is used to estimate HR and RR. However, since time domain information is sensitive to even small noise, this simple algorithm identifies invalid peaks as a signal period resulting in inaccurate estimation. Liu et al. [70] used a threshold to filter out invalid peaks with low amplitude differences between the peak of waveform and valley. Yamamoto et al. [42] found the phase change of heartbeat may not keep at the same location (it may appear at adjacent locations), so they used the Viterbi algorithm to locate peaks that phase change at different locations and prevent losing the heartbeat. In Reference [109], the Kalman filter was introduced for heart-rate tracking. They used the estimate and uncertainty further to update and narrow band-pass, aiming at reducing invalid peaks. Actually, the time-domain algorithm is easier to obtain the **inter-beat-interval (IBI)** for calculating HRV indicator [74], e.g., **root mean square of successive differences (RMSSD)**, the standard deviation of all the IBIs (SDRR) and the percentage of successive IBIs that differ by more than 50 ms (pNN50).

From the frequency domain, the accuracy of the RR and HR estimation is dependent on the length of the observation window and the selection of frequency peak. FFT [54] and **continuous**

**wavelet transform (CWT)** [84, 89] are effective and widely applicable spectral analysis methods. However, FFT and CWT do not perform well at low SNR due to fake peaks.

To take advantage of both time domain and frequency domain information, Ahmad et al. [68] calculated the confidence coefficient of the respiratory signal spectrum, and the inter-peak distance-based method was chosen to estimate the vital signs if the confidence coefficient is below a certain threshold. Wang et al. [92] proposed to first estimate the reference heart rate in the time domain on the data with the rapidly changing part in. Spectral analysis is then performed, and the final estimated HR is searched in the frequency neighborhood of the reference heart rate. In addition, **auto-regressive (AR)** [86, 90] and cross-correlation [104] methods were also used to estimate HR and RR.

**5.3.2 BP Estimation.** Blood pressure can be measured by a sphygmomanometer in clinical medicine. The sphygmomanometer stops the blood flow in the local artery by inflating the cuff to increase pressure. At that point, the cuff pressure equals the BP. This method requires an inflated cuff and is not suitable for continuous detection. **Pulse transit time (PTT)** [110] or **pulse wave velocity (PWV)** [111] is a promising method for the noninvasive and continuous detection of BP. They provide the opportunity to estimate cuffless arterial BP. PWV is the transit velocity of blood pulse waves through the arterial system. It is very challenging to measure PWV directly, while indirect measurement of PWV via PTT is easier to achieve. PTT is the pulse delay between two known places on the artery and is an indirect parameter measuring PWV. The conventional method to calculate PTT is using at least two signals generated by the cardiovascular system, for example, the interval between the R-peak of the ECG signal and the foot of the PPG signal [112]. However, BP cannot be accurately measured from the PTT alone. Guyton et al. [113] demonstrated the relationship between cardiac output and arterial pressure control. BP is the product of cardiac output and peripheral resistance. When BP decreases, HR increases in an effort to increase cardiac output, and the arterial walls contract to increase BP. Inspired by Reference [113], Wang et al. [114] correlated BP with HR and previous BP and formulate the BP estimation function as:

$$BP_n = a \cdot \ln PPT + b \cdot HR + c \cdot BP_{n-1} + d, \quad (30)$$

where  $BP_{n-1}$  is the previous BP estimate. The four coefficients ( $a$ ,  $b$ ,  $c$ , and  $d$ ) can be calculated by the least square method.

In non-contact BP detection, researchers try to use radar to estimate PTT. Buxi et al. [115] used electrical bioimpedance and CW radar to measure PTT and used linear regression method to estimate **systolic BP (SBP)**.

$$SBP = PPT \cdot a_1 + a_2, \quad (31)$$

where  $a$  and  $b$  are linear regression coefficients.

In Buxi's work [115], the contact electrode is still used. Tang et al. [116] proposed an all-radar-based detection approach. The author designed a single-frequency CW radar that operates concurrently with two different modes to estimate PTT without contact. One is SIL CW mode to detect the wrist pulse wave. The other is the CW mode to detect heartbeat waves. In this work. The **peak time difference (PTD)** between the two radar output signals is used to estimate PTT. The author experimentally demonstrated PTD has a good linear relationship with PTT.

## 5.4 Scenarios and Challenges of mmWave-based Vital Signs Detection

Although mmWave sensing technology is promising for vital signs detection, there may still be some limitations and challenges in practical applications. In this subsection, we discuss these practical scenarios and issues.

**5.4.1 Effects of MmWave Radiation.** As mmWave devices are to be widely deployed in the human living environment, users are most concerned about their safety issues, human exposure limits, and radiation damage. In fact, mmWave radiation is relatively low-energy, with photon energies ranging only from 0.1 to 1.2 meV, far short of the 12 eV required to break molecular bonds [117]. Thus, unlike ionizing radiation such as X-rays or ultraviolet light, which can cause cancer, mmWave radiation is non-ionizing. And the studies currently being conducted on the effects of mmWave radiation on the human body are more concerned with the effects of the thermal effect of the absorption of mmWave energy by body tissues resulting in a rise in temperature. Studies suggest that there is no significant temperature rise in the skin for longer exposures at low mmWave human exposure limits ( $< 1\text{mW/cm}^2$ ) [118]. Currently, the **International Electrotechnical Commission (IEC)** has developed relevant standards. The IEC standard for mmWave radiation human exposure limit is  $0.1\text{mW/cm}^2$  [119]. Adhering to mmWave equipment that meets this standard effectively mitigates potential safety concerns, ensuring the protection of users in practical applications.

**5.4.2 Relative Position of mmWave Device and Subject.** The relative positions of mmWave devices and targets may cause challenges in vital signs estimation, which include **radar cross-section (RCS)** reduction, mmWave attenuation, occlusion by stationary objects, and strong multipath effects in NLOS scenarios. The most common experimental scenario in current related work involves subjects sitting on a chair facing a mmWave device placed at a certain height. Iyer et al. [120] positioned an FMCW radar at approximately 1 meter above the ground to investigate the impact of subject orientation and distance on vital sign estimation. The experiments reveal that errors increase when the subject is side-facing the radar due to a smaller RCS. In addition, the attenuation properties of wave result in an inability to consistently detect vital signs when the subject is more than 1.5 meters away from the radar, which is consistent with the experimental results in References [121, 122]. Ren et al. [121] also compared vital sign estimation under three conditions: subjects wearing only a cotton T-shirt, subjects wearing a T-shirt and a wool sweater, and subjects wearing a T-shirt, sweater, and polyester jacket. The results showed that the error rate was less than 3% compared to subjects not wearing clothes. In practical scenarios, subjects will have the possibility of being occluded in addition to not facing the radar head-on. In this NLOS scenario, the vital sign signal is very weak and vital sign detection is affected by strong multipath effects. Li et al. [123] explored the extraction of respiratory signals in a relatively simple NLOS scenario, i.e., in an L-shaped corridor. Their model considered only one signal reflection. More complex multipath environment remains to be addressed. In addition to placing mmWave devices at a certain height above the ground, some studies install mmWave devices on the ceiling to monitor the vital signs of bedridden patients [53, 124]. This approach effectively avoids the issue of large vital sign estimation errors caused by object obstruction. However, the ceiling-mounted mmWave device is easily interfered by the healthcare worker's body movement when the healthcare worker approaches the patient's bedside. To address this interference issue, Lim et al. [125] mounted mmWave device on the back of the bed. To find the most suitable observation position with minimal interference from random body movements for drivers in small vehicles, researchers in Reference [126] compared the performance of 16 different positions of UWB radar in vehicles. The experiments showed that the rearview mirror was a reliable position for measuring vital signs. In summary, when deploying mmWave devices, the relative positions of mmWave devices and targets should be selected according to actual requirements. Overall, the performance of the sensing algorithm is more effective when mmWave devices are placed in a position with a clear line of sight, minimal obstructions, and ideally facing the subjects.

**5.4.3 Multi-subject and Random Body Movement.** Multi-subject vital signs detection and randomness of human motion are long-standing unsolved challenges. Multi-subject vital signs detection imposes higher hardware requirements on mmWave devices to separate targets with improved distance and angular resolution. And random body motion can severely distort the radar signal and affect the extraction of cardiac features. Much of the current work claiming to allow for multi-target vital signs detection focuses on separating multiple stationary targets sitting in close proximity to each other in the dimensions of distance, azimuth, elevation, and Doppler frequency, and thus estimating vital signs separately [68, 73, 74, 127]. Such schemes obviously do not work in real scenarios. This is because they do not take into account user movement, nor do they take into account the situation where the user enters or leaves the radar field of view. To track multiple users in the radar field of view, Mercuri et al. [18] tracked users with Doppler velocities through a point-to-point multiplication of the velocity matrix at the range matrix. Zhang et al. [128] tracked multiple users using a graph path selection algorithm on the range-azimuth map. However, they attempt to estimate the target's vital signs only when the tracking target remains stationary. This is because when the target is moving, random body movements cause the vital sign signal to be drowned out. To address the problem of random body movements of the driver in the cockpit affecting vital sign estimation, Wang et al. [4] designed a two-step motion compensation algorithm. It is first based on computing a 2D cross-correlation on a sequence of range-azimuth maps, aligning the sequence of range-azimuth maps to remove large body displacements, and then further removing subtle motion artifacts using the smoothing spline method. Zhang et al. [129] used two IR-UWB radars to collect echo data from the chest and abdomen, respectively. Random body motion effects were mitigated by calculating the correlation of vital signals decomposed from the two radars. These solutions, while mitigating the effects of random body motion to some extent, are specific to a single target. Currently, solutions that can be used in real-life scenarios, i.e., solutions for multi-user vital sign detection without static constraints, require further research. Combined cameras could be a potential solution. First, the cameras provide more accurate multi-target localization tracking than mmWave sensors, and second, through identification, historical vital signs information of the target can be utilized.

**5.4.4 Public Datasets.** In the field of mmWave-based vital signs detection, most researchers tend to collect their own small-scale datasets to validate their methods, because their proposed methods do not require pretraining on a dataset. However, the deep learning-based methods mentioned in the later section need to rely on large-scale datasets. Recently, Yoo et al. [130] provided a dataset from 50 children aged less than 13 years old. This dataset was recorded by the FMCW radar while the subjects were at rest and provided the reference HR and RR. Shi et al. [131] provided a 223-minute-long dataset recorded by a CW radar. This dataset was collected with subjects lying flat on their backs, with 11 individuals participating, and provided synchronized acquisition of ECG signals. These datasets can help researchers to validate the effectiveness of algorithms in the early design stage, but we still need massive datasets in multiple scenarios to cope with the complexity of real scenarios. We call on researchers to produce public datasets for multiple scenarios, such as multi-subject scenarios, random motion scenarios, and so on, to benefit the development of mmWave-based vital sign detection technology.

## 6 DEEP LEARNING-BASED MVSS

Recent years have witnessed that deep learning is widely applied in wireless sensing due to the advancements in big data and computing. Deep learning can cope with the potentially massive noise of wireless signals, break through the limited pattern representation of traditional signal processing techniques, and extract high-level features from raw data. And by leveraging deep

Table 4. Summary of Related Research Applying Deep Learning

Status	Region of interest	Architecture	Model input	Model output	Performance	
[134]	Static	Lower leg	CNN	Processed phase signal	Accuracy of over 90%	
[135]	Static	Chest	LSTM	I/Q data	Relative errors around 5%	
[75]	Static	Chest	CNN Unet	Processed phase signal SCG-like waveform	Highest correlation of 90% Median error between 0.26%-1.2%	
[93]	Static	Chest	Encoder-decoder	4D measurements	Median Pearson-Correlation of 90%	
[137]	Restricted movement	Chest	VED	I/Q data	Average cosine similarity of 91.62%	
[138]	Restricted movement	Chest	MLP Encoder-decoder	CIR matrix Separated Patterns	Separated Patterns Vital signs waveform	Cosine similarity of over 80%
[136]	Free movement	Full body	LSTM	Movement power	HR, RR	Mean error of 5.57 bpm for HR and 3.32 bpm for RR
[59]	Free movement	Chest	LSTM	CaSE features	ECG-like waveform	Mean correlation coefficients of over 90%

learning, the performance of various wireless sensing applications (e.g., gesture recognition [132], fall detection [133]) has been further enhanced so wireless sensing is becoming a new approach for perceiving the world. And in the research field of MVSS, deep learning is also widely used in the aspect of estimating HR, RR, and HRV [75, 134–136], reconstructing waveforms [59, 75, 93, 137, 138], canceling out motion interference [59, 136–138], and so on. We briefly classify the papers mentioned in this section into three categories based on their ability to handle body movements. [75, 93, 134, 135] demand that the human subject stationary [137, 138], deliver a solution when the target is under restricted movement. It is under free movement that Reference [59, 136] make attempts to detect the subject's vital signs. In Table 4, we present a comparison of their details.

Zhao et al. [134] proposed mBeats, a **convolutional neural network (CNN)**-based system that provided periodic HR measurements. mBeats focuses on the phase variation signals on the user's lower leg, which is then filtered and fed to a CNN consisting of three lightweight 1D convolutional layers and two fully connected layers. It is noteworthy to mention that the CNN predicts not only the HR but also a confidence interval. Experiments show that the CNN with uncertainty estimation achieves an accuracy of 93.85% and 93.03% on two different targets, respectively. In Reference [75], the CNN-assisted template matching method was utilized to extract HR from the phase variation signals pre-processed by the differentiator filter. The architecture consists of a 1D convolutional layer that learns a template as its convolutional filter and a Maxpool layer that attempts to find peaks indicating the number of heartbeats from the output of the previous layer. The authors note that their method is linear in time and has high accuracy with minimal parameters. Shi et al. [135] proposed a contactless HRV monitoring system that used **long short-term memory (LSTM)** networks with two bidirectional LSTM layers for the heart sound segmentation task. And the two bidirectional LSTM layers containing 400 hidden cells and 200 hidden cells, respectively, can capture the bi-directional state of the heart sound signal. Experiments show that the relative error of extracted HRV indices, such as HF norm, is around 5%.

Although the above-mentioned research works achieve higher robustness and accuracy than conventional signal processing methods, they still only estimate HR and fail to provide the same level of detail as clinical gold standard heart recordings. And such heart recordings usually play a significant role in health monitoring and disease diagnosis. For instance, prolonged P wave duration on a standard 12-lead EGG is a marker of delayed inter-atrial conduction, which may predict cardiovascular disease [139]. And the following papers have attempted to reconstruct fine-grained waveforms to acquire critical physiological events.

RF-SCG [75] utilized a CNN consisting of three 1D convolutional layers to learn the mapping functions from RF signals to the SCG-like recordings. It is worth mentioning that a large number of signal processing methods, such as beamforming, FFT, differential filters, and so on, are applied to ensure that the RF signal input to the CNN is from the location of the heart. Experiments on 21 subjects show that the correlation coefficients of the SCG-like waveforms reconstructed from RF-SCG are all above 0.72. In addition, the authors use the U-net for automatic labeling of five cardiac events

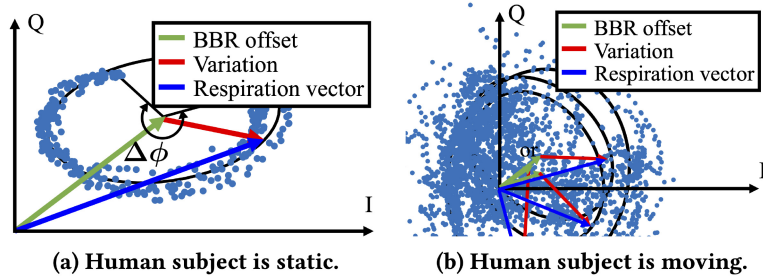


Fig. 13. Constellation diagrams of IQ signal [137].

in the reconstructed SCG-like waveforms with a median error between 0.26%–1.29%. Similar to RF-SCG, in the system proposed by Chen et al. [93], which provides ECG-like waveforms without contact, numerous algorithms are also used to obtain 4D measurements of the heart as input to the encoder-decoder-style neural network. Specifically, the encoder is a hybrid CNN-Transformer architecture that is aimed at exploiting the temporal and spatial features of 4D measurements. And the decoder is a temporal convolutional network that is used to compute all the ECG measurements. And experiments indicate that the reconstructed ECG-like waveform achieves timing accuracy of cardiac electrical events with a median error below 14 ms, morphology accuracy with a median Pearson-Correlation of 90%, and median Root-Mean-Square-Error of 0.081 mv.

It is when the target remains relatively stationary that the aforementioned two research works are able to reconstruct fine-grained waveforms. But in reality, it is impractical to force a subject to remain static during monitoring. Therefore, it is imperative to extract vital signs with motion-robustness to adapt to more scenarios. Zheng et al. [137] visualized IQ signals under different target states and concluded that traditional signal processing methods (e.g., VMD, EMD) fail to properly handle the IQ scrambling and fast-time crossing issues of large-scale movements. As shown in Figure 13, when the human subject is moving, the respiratory vector is no longer as identifiable and analytical as when the human subject is at rest. Therefore, they resort to deep learning techniques.

MoRe-Fi [137] utilized a so-called **Variational Encoder-Decoder (VED)** to reconstruct fine-grained respiratory waveforms under restricted movement. The VED receives the I/Q data as two streams and encodes them separately as continuous probability distributions instead of discrete vector sets to handle out-of-range inputs. Then the resulting latent representations are aligned and fed to the decoder to recover respiratory waveform by minimizing the reconstruction error. Experiments show that the average cosine similarity between the recovered and ground truth is 0.9162. Chen et al. [138] attempted to use deep contrastive learning to distinguish between vital sign reflections and body motion reflections that are mixed in a nonlinear manner. The authors utilize different comparison strategies depending on the motion patterns. Specifically, for stationary motion (e.g., typing and walking on a treadmill), the original time sequences and their random versions are compared, and for non-stationary motion (e.g., standing up or sitting down abruptly), distinct time segments of the same original time sequences are compared. After pre-training, the resulting time sequences are refined and merged using the encoder-decoder module to recover the vital sign waveforms.

To date, most MVSS systems operate under controlled conditions (i.e., the target is stationary or motion-limited). For example, Reference [138] requires that the variable range between the radar and the subject lies within a reasonable range (e.g., 50 cm) and that the human subject remains within the FoV of radar. The next two papers seem to propose novel methods for isolating motion artifacts to detect vital signs under free body movement.

Gong et al. [136] utilized two customized LSTM networks to find sophisticated correlations between RF signal patterns, motion power, and vital signs (RR and HR). The RR LSTM consists of two stacked LSTMs: one receiving motion power for motion pattern classification as well as the other receiving motion patterns and motion power for RR estimation. The HR model accepts a closed-form movement power as input and outputs real-time HR. To achieve cross-subjects generalization, Reference [136] incorporates two mechanisms: instant calibration and adaptive training, for calibrating the error of every single period of movement and long-term generalization error, respectively. Experiments involving multiple subjects show that the mean estimation error for HR is 5.57 bpm and for RR is 3.32 bpm. Xu et al. [59] proposed CardiacWave, a **cardiac-mmWave scattering effect (CaSE)**-based system that provides contactless ECG-like waveforms. Compared to most MVSS systems that measure chest displacement, it is less subject to motion interference. CardiacWave has two main components. The first one is a masking filter with learning coefficients, which aims to extract case features from frequency shifts to represent cardiac electrical activity information. The other one is an architecture combining LSTM and an attention module for extracting integral information from CaSE features and retrieving long-term cardiac activity information. And experiments indicate that the timing difference of P-waves, T-waves, and QRS complex is 0.67%, 0.71%, and 0.49%, respectively, and a mean cardiac event difference is within a delay of 5.3 milliseconds.

## 7 CONCLUSION

In this survey, we primarily concentrate on vital sign-related content, including human anatomy and various measurement methods (both contact and non-contact). We then discuss four MVSS signal models and the signal processing chain for MVSS. Moreover, we highlight the role of deep learning in the field of MVSS and compare current related studies. Specific applications of MVSS are also examined.

From our survey, it is evident that radar-based methods for sensing vital signs have garnered significant attention. However, there are still aspects that can be further explored:

**Movement cancellation and multiple targets:** Much research has been devoted to refining the granularity of sensing outcomes for a single, static target. However, in real-life scenarios, there are often multiple targets with a wide range of random motions. Addressing the challenge of vital sign monitoring with multi-target motion robustness is an urgent open problem.

**Multi-modality:** Multimodal techniques ensure that the system functions correctly by utilizing information from other modalities when one modality fails to provide clear information. Additionally, fusing multimodal information allows one modality to compensate for the shortcomings of another, resulting in more accurate and robust vital sign estimates. For example, body echoes captured by mmWave radar can replace RGB imaging as the primary reference information when the lighting environment is suboptimal or the target is obscured. Moreover, combining blood volume changes extracted from RGB images with chest displacement extracted from echoes may provide a better representation of cardiac activity.

**Deep learning:** Recent studies in the field of MVSS show that deep learning effectively enhances radar-based vital sign sensing. However, few studies exploit deep learning's powerful feature fusion capabilities to integrate multimodal feature information for a more comprehensive portrayal of human physiological activity. Additionally, there is a lack of large-scale and annotated public radar datasets in the field of MVSS. Therefore, automatic labeling of MVSS data and representation learning from unlabeled data will likely become future research trends in this area.

**Applications based on MVSS:** When fine-grained vital waveforms can be robustly acquired via radar, it is natural to consider extracting various features for diverse applications. Disease

diagnosis, biometric authentication, and emotional health are considered three promising applications in this context.

## REFERENCES

- [1] Fortune Business Insights. Remote Patient Monitoring Devices Market, Global Report [2028]. Retrieved from <https://www.fortunebusinessinsights.com/remote-patient-monitoring-devices-market-106328>
- [2] World Health Organization. Cardiovascular diseases (CVDs). Retrieved from [https://www.who.int/en/news-room/fact-sheets/detail/cardiovascular-diseases-\(cvds\)](https://www.who.int/en/news-room/fact-sheets/detail/cardiovascular-diseases-(cvds))
- [3] World Health Organization. Noncommunicable diseases. Retrieved from <https://www.who.int/news-room/fact-sheets/detail/noncommunicable-diseases>
- [4] Fengyu Wang, Xiaolu Zeng, Chenshu Wu, Beibei Wang, and K. J. Ray Liu. 2022. Driver vital signs monitoring using millimeter wave radio. *IEEE Internet of Things Journal* 9, 13 (2022), 11283–11298.
- [5] Shiyu Wu, Siqi Yao, Wei Liu, Kai Tan, Zhenghuan Xia, Shengwei Meng, Jie Chen, Guangyou Fang, and Hejun Yin. 2016. Study on a novel UWB linear array human respiration model and detection method. *IEEE J. Select. Topics Appl. Earth Observ. Rem. Sens.* 9, 1 (2016), 125–140.
- [6] Peipei Cao, Weijie Xia, and Yi Li. 2019. Heart ID: Human identification based on radar micro-doppler signatures of the heart using deep learning. *Rem. Sens.* 11, 10 (2019), 1220.
- [7] Yang Han, Timo Lauteslager, Tor S. Lande, and Timothy G. Constandinou. 2019. UWB radar for non-contact heart rate variability monitoring and mental state classification. In *41st Annual International Conference of the IEEE Engineering in Medicine and Biology Society (EMBC'19)*. IEEE, 6578–6582.
- [8] Vinh Phuc Tran, Adel Ali Al-Jumaily, and Syed Mohammed Shamsul Islam. 2019. Doppler radar-based non-contact health monitoring for obstructive sleep apnea diagnosis: A comprehensive review. *Big Data Cognit. Comput.* 3, 1 (2019), 3.
- [9] Steffen Leonhardt, Lennart Leicht, and Daniel Teichmann. 2018. Unobtrusive vital sign monitoring in automotive environments—A review. *Sensors* 18, 9 (2018), 3080.
- [10] Emanuele Cardillo and Alina Caddemi. 2020. A review on biomedical MIMO radars for vital sign detection and human localization. *Electronics* 9, 9 (2020), 1497.
- [11] Mamady Kebe, Rida Gadhafi, Baker Mohammad, Mihai Sanduleanu, Hani Saleh, and Mahmoud Al-Qutayri. 2020. Human vital signs detection methods and potential using radars: A review. *Sensors* 20, 5 (2020), 1454.
- [12] Anuradha Singh, Saeed Ur Rehman, Sira Yongchareon, and Peter Han Joo Chong. 2020. Multi-resident non-contact vital sign monitoring using radar: A review. *IEEE Sensors J.* 21, 4 (2020), 4061–4084.
- [13] Ameen Bin Obadi, Ping Jack Soh, Omar Aldayel, Muataz Hameed Al-Doori, Marco Mercuri, and Dominique Schreurs. 2021. A survey on vital signs detection using radar techniques and processing with FPGA implementation. *IEEE Circ. Syst. Mag.* 21, 1 (2021), 41–74.
- [14] Giacomo Paterniani, Daria Sgreccia, Alessandro Davoli, Giorgio Guerzoni, Pasquale Di Vести, Anna Chiara Valenti, Marco Vitolo, Giorgio M. Vitetta, and Giuseppe Boriani. 2023. Radar-based monitoring of vital signs: A tutorial overview. *Proceedings of the IEEE* 111, 3 (2023), 277–317.
- [15] Jia Zhang, Rui Xi, Yuan He, Yimiao Sun, Xiuzhen Guo, Weiguo Wang, Xin Na, Yunhao Liu, Zhenguo Shi, and Tao Gu. 2023. A survey of mmWave-based human sensing: Technology, platforms and applications. *IEEE Communications Surveys & Tutorials*, 1–1.
- [16] Fred Shaffer, Rollin McCraty, and Christopher L. Zerr. 2014. A healthy heart is not a metronome: An integrative review of the heart's anatomy and heart rate variability. *Front. Psychol.* 5 (2014), 1040.
- [17] R. E. Klabunde. 2011. *Cardiovascular Physiology Concepts*. Lippincott Williams & Wilkins, Baltimore, MD.
- [18] Marco Mercuri, Ilde Rosa Lorato, Yao-Hong Liu, Fokko Wieringa, Chris Van Hoof, and Tom Torfs. 2019. Vital-sign monitoring and spatial tracking of multiple people using a contactless radar-based sensor. *Nat. Electron.* 2, 6 (2019), 252–262.
- [19] Eric Awtry, Cathy Jeon, and Molly G. Ware. 2006. *Blueprints Cardiology*. Lippincott Williams & Wilkins.
- [20] C. Barr Taylor. 2010. Depression, heart rate related variables and cardiovascular disease. *Int. J. Psychophysiol.* 78, 1 (2010), 80–88.
- [21] Paolo Melillo, Marcello Bracale, and Leandro Peccia. 2011. Nonlinear heart rate variability features for real-life stress detection. Case study: Students under stress due to university examination. *Biomed. Eng. Online* 10, 1 (2011), 1–13.
- [22] Richard Drake, A. Wayne Vogl, and Adam W. M. Mitchell. 2009. *Gray's Anatomy for Students E-book*. Elsevier Health Sciences.
- [23] C. Loring Brace. 2002. Anatomy & physiology: The unity of form and function. *JSTOR 2002*, Vol. 77.
- [24] Richard M. Leach. 2008. Symptoms and signs of respiratory disease. *Medicine* 36, 3 (2008), 119–125.

- [25] Flávio D. Fuchs and Paul K. Whelton. 2020. High blood pressure and cardiovascular disease. *Hypertension* 75, 2 (2020), 285–292.
- [26] Bryan Williams, Giuseppe Mancia, Wilko Spiering, Enrico Agabiti Rosei, Michel Azizi, Michel Burnier, Denis L. Clement, Antonio Coca, Giovanni de Simone, Anna Dominiczak, Thomas Kahan, Felix Mahfoud, Josep Redon, Luis Ruilope, Alberto Zanchetti, Mary Kerins, Sverre E. Kjeldsen, Reinhold Kreutz, Stephane Laurent, Gregory Y. H. Lip, Richard McManus, Krzysztof Narkiewicz, Frank Ruschitzka, Roland E. Schmieder, Evgeny Shlyakhto, Costas Tsiofis, Victor Aboyans, Illeana Desormais, and ESC Scientific Document Group. 2018. 2018 ESC/ESH guidelines for the management of arterial hypertension: The task force for the management of arterial hypertension of the European Society of Cardiology (ESC) and the European Society of Hypertension (ESH). *European Heart Journal* 39, 33 (2018), 3021–3104.
- [27] Majd AlGhatrif and Joseph Lindsay. 2012. A brief review: History to understand fundamentals of electrocardiography. *J. Commun. Hosp. Intern. Med. Perspect.* 2, 1 (2012), 14383.
- [28] Marcus Schmidt, Andy Schumann, Jonas Mueller, Karl-Juergen Baer, and Georg Rose. 2017. ECG derived respiration: Comparison of time-domain approaches and application to altered breathing patterns of patients with schizophrenia. *Physiol. Measur.* 38, 4 (2017), 601.
- [29] R. P. Paiva, P. Carvalho, R. Couceiro, J. Henrique, M. Antunes, I. Quintal, and J. Muehlsteff. 2012. Beat-to-beat systolic time-interval measurement from heart sounds and ECG. *Physiol. Measur.* 33, 2 (2012), 177.
- [30] Pierre-François Migeotte, Sven De Ridder, Jens Tank, Nathalie Pattyn, Irina Funtova, R. Baevsky, Xavier Neyt, and Gordon Kim Prisk. 2012. Three dimensional ballisto-and seismo-cardiography: HIJ wave amplitudes are poorly correlated to maximal systolic force vector. In *Annual International Conference of the IEEE Engineering in Medicine and Biology Society*. IEEE, 5046–5049.
- [31] John Allen. 2007. Photoplethysmography and its application in clinical physiological measurement. *Physiol. Measur.* 28, 3 (2007), R1.
- [32] Marc Garbey, Nanfei Sun, Arcangelo Merla, and Ioannis Pavlidis. 2007. Contact-free measurement of cardiac pulse based on the analysis of thermal imagery. *IEEE Trans. Biomed. Eng.* 54, 8 (2007), 1418–1426.
- [33] Ramya Murthy and Ioannis Pavlidis. 2006. Noncontact measurement of breathing function. *IEEE Eng. Med. Biol. Mag.* 25, 3 (2006), 57–67.
- [34] Mayank Kumar, Ashok Veeraraghavan, and Ashutosh Sabharwal. 2015. DistancePPG: Robust non-contact vital signs monitoring using a camera. *Biomed. Opt. Expr.* 6, 5 (2015), 1565–1588.
- [35] Xijian Fan, Qiaolin Ye, Xubing Yang, and Sruti Das Choudhury. 2020. Robust blood pressure estimation using an RGB camera. *J. Amb. Intell. Human. Comput.* 11, 11 (2020), 4329–4336.
- [36] Kun Qian, Chenshu Wu, Fu Xiao, Yue Zheng, Yi Zhang, Zheng Yang, and Yunhao Liu. 2018. Acousticcardiogram: Monitoring heartbeats using acoustic signals on smart devices. In *IEEE Conference on Computer Communications*. IEEE, 1574–1582.
- [37] Anran Wang, Dan Nguyen, Arun R. Sridhar, and Shyamnath Gollakota. 2021. Using smart speakers to contactlessly monitor heart rhythms. *Commun. Biol.* 4, 1 (2021), 1–12.
- [38] G. Cosoli, L. Casacanditella, E. P. Tomasini, and L. Scalise. 2015. Evaluation of heart rate variability by means of laser doppler vibrometry measurements. In *Journal of Physics: Conference Series*, Vol. 658. IOP Publishing, 012002.
- [39] Jessi E. Johnson, Oliver Shay, Chris Kim, and Catherine Liao. 2019. Wearable millimeter-wave device for contactless measurement of arterial pulses. *IEEE Trans. Biomed. Circ. Syst.* 13, 6 (2019), 1525–1534.
- [40] Karthik Ramasubramanian and Kishore Ramaiah. 2018. Moving from legacy 24 GHz to state-of-the-art 77-GHz radar. *ATZelektron. Worldw.* 13, 3 (2018), 46–49.
- [41] Yonggu Lee, Jun-Young Park, Yeon-Woo Choi, Hyun-Kyung Park, Seok-Hyun Cho, Sung Ho Cho, and Young-Hyo Lim. 2018. A novel non-contact heart rate monitor using impulse-radio ultra-wideband (IR-UWB) radar technology. *Scient. Rep.* 8, 1 (2018), 1–10.
- [42] Kohei Yamamoto, Koji Endo, and Tomoaki Ohtsuki. 2021. Remote sensing of heartbeat based on space diversity using MIMO FMCW Radar. In *IEEE Global Communications Conference (GLOBECOM’21)*. IEEE, 1–6.
- [43] Lingyun Ren, Lingqin Kong, Farnaz Foroughian, Haofei Wang, Paul Theilmann, and Aly E. Fathy. 2017. Comparison study of noncontact vital signs detection using a Doppler stepped-frequency continuous-wave radar and camera-based imaging photoplethysmography. *IEEE Trans. Microw. Theor. Techniq.* 65, 9 (2017), 3519–3529.
- [44] Fusang Zhang, Daqing Zhang, Jie Xiong, Hao Wang, Kai Niu, Beihong Jin, and Yuxiang Wang. 2018. From Fresnel diffraction model to fine-grained human respiration sensing with commodity Wi-Fi devices. *Proc. ACM Interact. Mob. Wear. Ubiq. Technol.* 2, 1 (2018), 1–23.
- [45] Peter Hillyard, Anh Luong, Alemayehu Solomon Abrar, Neal Patwari, and Sarah Hatch Pollard. 2018. Experience: Cross-technology radio respiratory monitoring performance study. In *24th Annual International Conference on Mobile Computing and Networking*.

- [46] Dingyang Wang, Sungwon Yoo, and Sung Ho Cho. 2020. Experimental comparison of IR-UWB radar and FMCW radar for vital signs. *Sensors* 20, 22, 6695 (2020), 1–22.
- [47] Faheem Khan, Asim Ghaffar, Naeem Khan, and Sung Ho Cho. 2020. An overview of signal processing techniques for remote health monitoring using impulse radio UWB transceiver. *Sensors* 20, 9 (2020), 2479.
- [48] Xiaolin Liang, Jianqin Deng, Hao Zhang, and Thomas Aaron Gulliver. 2018. Ultra-wideband impulse radar through-wall detection of vital signs. *Scientific Reports*, 8, 1 (2018), 13367.
- [49] Xiaolin Liang, Tingting Lv, Hao Zhang, Yong Gao, and Guangyou Fang. 2018. Through-wall human being detection using UWB impulse radar. *EURASIP J. Wirel. Commun. Netw.* 2018, 1 (2018), 46.
- [50] Yu Rong, Panagiotis C. Theofanopoulos, Georgios C. Trichopoulos, and Daniel W. Bliss. 2020. Cardiac sensing exploiting an ultra-wideband terahertz sensing system. In *IEEE International Radar Conference (RADAR'20)*.
- [51] Yu Rong, Panagiotis C. Theofanopoulos, Georgios C. Trichopoulos, and Daniel W. Bliss. 2022. A new principle of pulse detection based on terahertz wave plethysmography. *Scientific Reports*, 12, 1 (2022), 6347.
- [52] Fu-Kang Wang, Chung-Tse Michael Wu, Tzyy-Sheng Horng, Chao-Hsiung Tseng, Shiang-Hwu Yu, Chia-Chan Chang, Pin-Hsun Juan, and Yichao Yuan. 2020. Review of self-injection-locked radar systems for noncontact detection of vital signs. *IEEE J. Electromag., RF Microw. Med. Biol.* 4, 4 (2020), 294–307.
- [53] Mostafa Alizadeh, George Shaker, João Carlos Martins De Almeida, Plinio Pelegrini Morita, and Safeddin Safavi-Naeini. 2019. Remote monitoring of human vital signs using mm-Wave FMCW radar. *IEEE Access* 7 (2019), 54958–54968.
- [54] Yong Wang, Wen Wang, Mu Zhou, Aihu Ren, and Zengshan Tian. 2020. Remote monitoring of human vital signs based on 77-GHz mm-Wave FMCW radar. *Sensors* 20, 10 (2020), 2999.
- [55] Yanhua Zhao, Vladica Sark, Milos Krstic, and Eckhard Grass. 2021. Multi-target vital signs remote monitoring using mmWave FMCW radar. In *IEEE Microwave Theory and Techniques in Wireless Communications (MTTW'21)*. IEEE, 290–295.
- [56] Parikha Mehrotra, Baibhab Chatterjee, and Shreyas Sen. 2019. EM-wave biosensors: A review of RF, microwave, mm-Wave and optical sensing. *Sensors* 19, 5 (2019), 1013.
- [57] J.-H. Park, C.-S. Kim, B.-C. Choi, and K.-Y. Ham. 2003. The correlation of the complex dielectric constant and blood glucose at low frequency. *Biosens. Bioelectron.* 19, 4 (2003), 321–324.
- [58] Simon H. Yueh, Richard West, William J. Wilson, Fuk K. Li, Eni G. Njoku, and Yahya Rahmat-Samii. 2001. Error sources and feasibility for microwave remote sensing of ocean surface salinity. *IEEE Trans. Geosci. Rem. Sens.* 39, 5 (2001), 1049–1060.
- [59] Chenhan Xu, Huining Li, Zhengxiong Li, Hanbin Zhang, Aditya Singh Rathore, Xingyu Chen, Kun Wang, Mingchun Huang, and Wenyao Xu. 2021. CardiacWave: A mmWave-based scheme of non-contact and high-definition heart activity computing. *Proc. ACM Interact. Mob. Wear. Ubiqu. Technol.* 5, 3 (2021), 1–26.
- [60] Marco Mercuri, Dominique Schreurs, and Paul Leroux. 2012. SFCW microwave radar for in-door fall detection. In *IEEE Topical Conference on Biomedical Wireless Technologies, Networks, and Sensing Systems (BioWireless'12)*. IEEE, 53–56.
- [61] Jack Capon. 1969. High-resolution frequency-wavenumber spectrum analysis. *Proc. IEEE* 57, 8 (1969), 1408–1418.
- [62] Otis Lamont Frost. 1972. An algorithm for linearly constrained adaptive array processing. *Proc. IEEE* 60, 8 (1972), 926–935.
- [63] Ralph Schmidt. 1986. Multiple emitter location and signal parameter estimation. *IEEE Trans. Antenn. Propag.* 34, 3 (1986), 276–280.
- [64] Richard Roy, A. Paulraj, and Thomas Kailath. 1986. Estimation of signal parameters via rotational invariance techniques-ESPRIT. In *IEEE Military Communications Conference: Communications-Computers: Teamed for the 90's (MILCOM'86)*, Vol. 3. IEEE, 41–6.
- [65] Ramdas Kumaresan and Donald W. Tufts. 1983. Estimating the angles of arrival of multiple plane waves. *IEEE Trans. Aerosp. Electron. Syst.* 1 (1983), 134–139.
- [66] Arthur Barabell. 1983. Improving the resolution performance of eigenstructure-based direction-finding algorithms. In *IEEE International Conference on Acoustics, Speech, and Signal Processing (ICASSP'83)*, Vol. 8. IEEE, 336–339.
- [67] Xian-Da Zhang and Ying-Chang Liang. 1995. Prefiltering-based ESPRIT for estimating sinusoidal parameters in non-Gaussian ARMA noise. *IEEE Trans. Sig. Process.* 43, 1 (1995), 349–353.
- [68] Adeel Ahmad, June Chul Roh, Dan Wang, and Aish Dubey. 2018. Vital signs monitoring of multiple people using a FMCW millimeter-wave sensor. In *IEEE Radar Conference (RadarConf'18)*. IEEE, 1450–1455.
- [69] Yong Jia, Yong Guo, Chao Yan, Haoxuan Sheng, Guolong Cui, and Xiaoling Zhong. 2019. Detection and localization for multiple stationary human targets based on cross-correlation of dual-station SFCW radars. *Rem. Sens.* 11, 12 (2019), 1428.

- [70] Kang Liu, Chenxu Ding, and Yuanhui Zhang. 2020. A coarse-to-fine robust estimation of FMCW radar signal for vital sign detection. In *IEEE Radar Conference (RadarConf'20)*. IEEE, 1–6.
- [71] Ingo Walterscheid, Oliver Biallawons, and Patrick Berens. 2019. Contactless respiration and heartbeat monitoring of multiple people using a 2-D imaging radar. In *41st Annual International Conference of the IEEE Engineering in Medicine and Biology Society (EMBC'19)*. IEEE, 3720–3725.
- [72] Yunus Emre Acar, Ismail Saritas, and Ercan Yaldiz. 2021. An experimental study: Detecting the respiration rates of multiple stationary human targets by stepped frequency continuous wave radar. *Measurement* 167 (2021), 108268.
- [73] Fengyu Wang, Feng Zhang, Chenshu Wu, Beibei Wang, and K. J. Ray Liu. 2020. ViMo: Multiperson vital sign monitoring using commodity millimeter-wave radio. *IEEE Internet Things J.* 8, 3 (2020), 1294–1307.
- [74] Fengyu Wang, Xiaolu Zeng, Chenshu Wu, Beibei Wang, and K. J. Ray Liu. 2021. mmHRV: Contactless heart rate variability monitoring using millimeter-wave radio. *IEEE Internet Things J.* 8, 22 (2021), 16623–16636.
- [75] Unsoo Ha, Salah Assana, and Fadel Adib. 2020. Contactless seismocardiography via deep learning radars. In *26th Annual International Conference on Mobile Computing and Networking*, 1–14.
- [76] Zhicheng Yang, Parth H. Pathak, Yunze Zeng, Xixi Liran, and Prasant Mohapatra. 2016. Monitoring vital signs using millimeter wave. In *17th ACM International Symposium on Mobile ad hoc Networking and Computing*, 211–220.
- [77] Xiaogang Yu, Changzhi Li, and Jenshan Lin. 2011. Two-dimensional noncontact vital sign detection using Doppler radar array approach. In *IEEE MTT-S International Microwave Symposium*. IEEE, 1–4.
- [78] Yu Rong, Arindam Dutta, Alex Chiriyath, and Daniel W. Bliss. 2021. Motion-tolerant non-contact heart-rate measurements from radar sensor fusion. *Sensors* 21, 5 (2021), 1774.
- [79] Changzhan Gu, Guochao Wang, Yiran Li, Takao Inoue, and Changzhi Li. 2013. A hybrid radar-camera sensing system with phase compensation for random body movement cancellation in Doppler vital sign detection. *IEEE Trans. Microw. Theor. Techniq.* 61, 12 (2013), 4678–4688.
- [80] Zi-Kai Yang, Heping Shi, Sheng Zhao, and Xiang-Dong Huang. 2020. Vital sign detection during large-scale and fast body movements based on an adaptive noise cancellation algorithm using a single Doppler radar sensor. *Sensors* 20, 15 (2020), 4183.
- [81] Xi Zhao, Chenyan Song, Victor Lubecke, and Olga Boric-Lubecke. 2011. DC coupled Doppler radar physiological monitor. In *Annual International Conference of the IEEE Engineering in Medicine and Biology Society*. IEEE, 1909–1912.
- [82] Changzhan Gu, Ruijiang Li, Hualiang Zhang, Albert Y. C. Fung, Carlos Torres, Steve B. Jiang, and Changzhi Li. 2012. Accurate respiration measurement using DC-coupled continuous-wave radar sensor for motion-adaptive cancer radiotherapy. *IEEE Trans. Biomed. Eng.* 59, 11 (2012), 3117–3123.
- [83] Ming-Chun Huang, Jason J. Liu, Wenya Xu, Changzhan Gu, Changzhi Li, and Majid Sarrafzadeh. 2015. A self-calibrating radar sensor system for measuring vital signs. *IEEE Trans. Biomed. Circ. Syst.* 10, 2 (2015), 352–363.
- [84] Xuyu Wang, Chao Yang, and Shiwen Mao. 2017. PhaseBeat: Exploiting CSI phase data for vital sign monitoring with commodity WiFi devices. In *IEEE 37th International Conference on Distributed Computing Systems (ICDCS'17)*. IEEE, 1230–1239.
- [85] Youwei Zeng, Dan Wu, Ruiyang Gao, Tao Gu, and Daqing Zhang. 2018. FullBreathe: Full human respiration detection exploiting complementarity of CSI phase and amplitude of WiFi signals. *Proc. ACM Interact. Mob. Wear. Ubiquitous Technol.* 2, 3 (2018), 1–19.
- [86] Youwei Zeng, Dan Wu, Jie Xiong, Enze Yi, Ruiyang Gao, and Daqing Zhang. 2019. FarSense: Pushing the range limit of WiFi-based respiration sensing with CSI ratio of two antennas. *Proc. ACM Interact. Mob. Wear. Ubiquitous Technol.* 3, 3 (2019), 1–26.
- [87] Marco Mercuri, Yiting Lu, Salvatore Polito, Fokko Wieringa, Yao-Hong Liu, Alle-Jan van der Veen, Chris Van Hoof, and Tom Torfs. 2021. Enabling robust radar-based localization and vital signs monitoring in multipath propagation environments. *IEEE Trans. Biomed. Eng.* 68, 11 (2021), 3228–3240.
- [88] Wansuree Massagram, Victor M. Lubecke, Anders HØst-Madsen, and Olga Boric-Lubecke. 2009. Assessment of heart rate variability and respiratory sinus arrhythmia via Doppler radar. *IEEE Trans. Microw. Theor. Techniq.* 57, 10 (2009), 2542–2549.
- [89] Toan K. Vo Dai, Kellen Oleksak, Tsotne Kvelashvili, Farnaz Foroughian, Chandler Bauder, Paul Theilmann, Aly E. Fathy, and Ozlem Kilic. 2021. Enhancement of remote vital sign monitoring detection accuracy using multiple-input multiple-output 77 ghz fmcw radar. *IEEE Journal of Electromagnetics, RF and Microwaves in Medicine and Biology* 6, 1 (2021), 111–122.
- [90] Hyunjae Lee, Byung-Hyun Kim, Jin-Kwan Park, and Jong-Gwan Yook. 2019. A novel vital-sign sensing algorithm for multiple subjects based on 24-GHz FMCW Doppler radar. *Rem. Sens.* 11, 10 (2019), 1237.
- [91] Qianlan Huang, Dawei Lu, Jiemin Hu, Hongqi Fan, Meirong Liang, and Jun Zhang. 2019. Simultaneous location and parameter estimation of human vital sign with MIMO-FMCW radar. In *IEEE International Conference on Signal, Information and Data Processing (ICSIDP'19)*. IEEE, 1–4.

- [92] Weicheng Wang, Zhenhua Jia, Chenren Xu, Guojie Luo, Daqing Zhang, Ning An, and Yanyong Zhang. 2021. Feasibility study of practical vital sign detection using millimeter-wave radios. *CCF Trans. Pervas. Comput. Interact.* 3, 4 (2021), 436–452.
- [93] Jinbo Chen, Dongheng Zhang, Zhi Wu, Fang Zhou, Qibin Sun, and Yan Chen. 2021. Contactless electrocardiogram monitoring with millimeter wave radar. *arXiv preprint arXiv:2112.06639* (2021).
- [94] Mi He, Yongjian Nian, and Yushun Gong. 2017. Novel signal processing method for vital sign monitoring using FMCW radar. *Biomed. Sig. Process. Contr.* 33 (2017), 335–345.
- [95] Jerome Gilles. 2013. Empirical wavelet transform. *IEEE Trans. Sig. Process.* 61, 16 (2013), 3999–4010.
- [96] James E. Fowler. 2005. The redundant discrete wavelet transform and additive noise. *IEEE Sig. Process. Lett.* 12, 9 (2005), 629–632.
- [97] Yunus Emre Acar, Ismail Saritas, and Ercan Yaldiz. 2021. An S-band zero-IF SFCW through-the-wall radar for range, respiration rate, and DOA estimation. *Measurement* 186 (2021), 110221.
- [98] Mi He, Yongjian Nian, Luping Xu, Lihong Qiao, and Wenwu Wang. 2020. Adaptive separation of respiratory and heartbeat signals among multiple people based on empirical wavelet transform using UWB radar. *Sensors* 20, 17 (2020), 4913.
- [99] Norden E. Huang, Zheng Shen, Steven R. Long, Manli C. Wu, Hsing H. Shih, Quanan Zheng, Nai-Chyuan Yen, Chi Chao Tung, and Henry H. Liu. 1998. The empirical mode decomposition and the Hilbert spectrum for nonlinear and non-stationary time series analysis. *Proc. R. Soc. Lond. Series A: Math., Phys. Eng. Sci.* 454, 1971 (1998), 903–995.
- [100] Fabio Weishaupt, Ingo Walterscheid, Oliver Biallawons, and Jens Klare. 2018. Vital sign localization and measurement using an LFMCW MIMO radar. In *19th International Radar Symposium (IRS'18)*. IEEE, 1–8.
- [101] Zhaohua Wu and Norden E. Huang. 2009. Ensemble empirical mode decomposition: A noise-assisted data analysis method. *Adv. Adapt. Data Anal.* 1, 01 (2009), 1–41.
- [102] María E. Torres, Marcelo A. Colominas, Gaston Schlotthauer, and Patrick Flandrin. 2011. A complete ensemble empirical mode decomposition with adaptive noise. In *IEEE International Conference on Acoustics, Speech and Signal Processing (ICASSP'11)*. IEEE, 4144–4147.
- [103] Li Sun, Shuaiming Huang, Yusheng Li, Chen Gu, Hao Pan, Hong Hong, and Xiaohua Zhu. 2020. Remote measurement of human vital signs based on joint-range adaptive EEMD. *IEEE Access* 8 (2020), 68514–68524.
- [104] Ching-Yao Huang, Guan-Wei Fang, Huey-Ru Chuang, and Chin-Lung Yang. 2019. Clutter-resistant vital sign detection using amplitude-based demodulation by EEMD-PCA-correlation algorithm for FMCW radar systems. In *49th European Microwave Conference (EuMC'19)*. IEEE, 928–931.
- [105] Lingyun Ren, Haofei Wang, Krishna Naishadham, Quanhua Liu, and Aly E. Fathy. 2015. Non-invasive detection of cardiac and respiratory rates from stepped frequency continuous wave radar measurements using the state space method. In *IEEE MTT-S International Microwave Symposium*. IEEE, 1–4.
- [106] Konstantin Dragomiretskiy and Dominique Zosso. 2013. Variational mode decomposition. *IEEE Trans. Sig. Process.* 62, 3 (2013), 531–544.
- [107] Zi Liang Xia, Xin Huai Wang, Hong Bo Wei, and Yin Xu. 2021. Detection of vital signs based on variational mode decomposition using FMCW radar. In *International Conference on Microwave and Millimeter Wave Technology (ICMWT'21)*. IEEE, 1–3.
- [108] Yuxuan Hu, Zhaoyang Xia, and Feng Xu. 2021. Using FMCW millimeter-wave radar to realize the detection of vital signs. In *International Conference on Microwave and Millimeter Wave Technology (ICMWT'21)*. IEEE, 1–3.
- [109] Muhammad Arsalan, Avik Santra, and Christoph Will. 2020. Improved contactless heartbeat estimation in FMCW radar via Kalman filter tracking. *IEEE Sensors Lett.* 4, 5 (2020), 1–4.
- [110] Andrew Steptoe, Harold Smulyan, and Brian Gribbin. 1976. Pulse wave velocity and blood pressure change: Calibration and applications. *Psychophysiology* 13, 5 (1976), 488–493.
- [111] Brian Gribbin, Andrew Steptoe, and Peter Sleight. 1976. Pulse wave velocity as a measure of blood pressure change. *Psychophysiology* 13, 1 (1976), 86–90.
- [112] X. F. Teng and Yuan-Ting Zhang. 2006. An evaluation of a PTT-based method for noninvasive and cuffless estimation of arterial blood pressure. In *International Conference of the IEEE Engineering in Medicine and Biology Society*. IEEE, 6049–6052.
- [113] Arthur C. Guyton. 1981. The relationship of cardiac output and arterial pressure control. *Circulation* 64, 6 (1981), 1079–1088.
- [114] Ruiping Wang, Wenyan Jia, Zhi-Hong Mao, Robert J. Sclabassi, and Mingui Sun. 2014. Cuff-free blood pressure estimation using pulse transit time and heart rate. In *12th International Conference on Signal Processing (ICSP'14)*. IEEE, 115–118.
- [115] Dilpreet Buxi, Jean-Michel Redouté, and Mehmet Rasit Yuce. 2016. Blood pressure estimation using pulse transit time from bioimpedance and continuous wave radar. *IEEE Trans. Biomed. Eng.* 64, 4 (2016), 917–927.

- [116] Mu-Cyun Tang, Chien-Min Liao, Fu-Kang Wang, and Tzzy-Sheng Horng. 2018. Noncontact pulse transit time measurement using a single-frequency continuous-wave radar. In *IEEE/MTT-S International Microwave Symposium (IMS'18)*. IEEE, 1409–1412.
- [117] Ting Wu, Theodore S. Rappaport, and Christopher M. Collins. 2015. Safe for generations to come: Considerations of safety for millimeter waves in wireless communications. *IEEE Microw. Mag.* 16, 2 (2015), 65–84.
- [118] Theodore S. Rappaport, Yunchou Xing, Ojas Kanhere, Shihao Ju, Arjuna Madanayake, Soumyajit Mandal, Ahmed Alkhateeb, and Georgios C. Trichopoulos. 2019. Wireless communications and applications above 100 GHz: Opportunities and challenges for 6G and beyond. *IEEE Access* 7 (2019), 78729–78757.
- [119] Congming Wang, Xiaohui Zhao, and Zan Li. 2023. Dcs-ctn: Subtle gesture recognition based on td-cnn-transformer via millimeter-wave radar. *IEEE Internet of Things Journal* 10, 20 (2023), 17680–17693.
- [120] Srikrishna Iyer, Leo Zhao, Manoj Prabhakar Mohan, Joe Jimeno, Mohammed Yakoob Siyal, Arokiaswami Alphones, and Muhammad Faeyz Karim. 2022. mm-Wave radar-based vital signs monitoring and arrhythmia detection using machine learning. *Sensors* 22, 9 (2022), 3106.
- [121] Lingyun Ren, Sabikun Nahar, Aly E. Fathy, Tuan Phan, Nghia Tran, and Ozlem Kilic. 2016. Investigation of vital signs monitoring errors due to subject's orientation, clothing and distance from a SFCW radar. In *IEEE International Symposium on Antennas and Propagation (APSURSI'16)*. IEEE, 1171–1172.
- [122] Sabikun Nahar, Tuan Phan, Farhan Quaiyum, Lingyun Ren, Aly E. Fathy, and Ozlem Kilic. 2018. An electromagnetic model of human vital signs detection and its experimental validation. *IEEE J. Emerg. Select. Topics Circ. Syst.* 8, 2 (2018), 338–349.
- [123] Gen Li, Yun Ge, Yiyu Wang, Qingwu Chen, and Gang Wang. 2022. Detection of human breathing in non-line-of-sight region by using mmWave FMCW radar. *IEEE Trans. Instrum. Measur.* 71 (2022), 1–11.
- [124] Jong Deok Kim, Won Hyuk Lee, Yonggu Lee, Hyun Ju Lee, Teahyen Cha, Seung Hyun Kim, Ki-Min Song, Young-Hyo Lim, Seok Hyun Cho, Sung Ho Cho, and Hyun-Kyung Park. 2019. Non-contact respiration monitoring using impulse radio ultrawideband radar in neonates. *Royal Society Open Science* 6, 6 (2019), 190149.
- [125] Sungmook Lim, Gwang Soo Jang, Wonyoung Song, Baek-hyun Kim, and Dong Hyun Kim. 2022. Non-contact VITAL signs monitoring of a patient lying on surgical bed using beamforming FMCW radar. *Sensors* 22, 21 (2022), 8167.
- [126] Zhicheng Yang, Maurizio Bocca, Vivek Jain, and Prasant Mohapatra. 2018. Contactless breathing rate monitoring in vehicle using UWB radar. In *7th International Workshop on Real-world Embedded Wireless Systems and Networks*. 13–18.
- [127] Zhi Li, Tian Jin, Yongpeng Dai, and Yongkun Song. 2021. Through-wall multi-subject localization and vital signs monitoring using UWB MIMO imaging radar. *Rem. Sens.* 13, 15 (2021), 2905.
- [128] Dongheng Zhang, Yang Hu, and Yan Chen. 2020. MTrack: Tracking multiperson moving trajectories and vital signs with radio signals. *IEEE Internet Things J.* 8, 5 (2020), 3904–3914.
- [129] Xinyue Zhang, Xizhu Yang, Yi Ding, Yili Wang, Jialin Zhou, and Lin Zhang. 2021. Contactless simultaneous breathing and heart rate detections in physical activity using IR-UWB radars. *Sensors* 21, 16 (2021), 5503.
- [130] Sungwon Yoo, Shahzad Ahmed, Sun Kang, Duhyun Hwang, Jungjun Lee, Jungduck Son, and Sung Ho Cho. 2021. Radar recorded child vital sign public dataset and deep learning-based age group classification framework for vehicular application. *Sensors* 21, 7 (2021), 2412.
- [131] Kilin Shi, Sven Schellenberger, Christoph Will, Tobias Steigleider, Fabian Michler, Jonas Fuchs, Robert Weigel, Christoph Ostgathe, and Alexander Koelpin. 2020. A dataset of radar-recorded heart sounds and vital signs including synchronised reference sensor signals. *Scient. Data* 7, 1 (2020), 50.
- [132] Saiwen Wang, Jie Song, Jaime Lien, Ivan Poupyrev, and Otmar Hilliges. 2016. Interacting with Soli: Exploring fine-grained dynamic gesture recognition in the radio-frequency spectrum. In *29th Annual Symposium on User Interface Software and Technology*. 851–860.
- [133] Na Lu, Yidan Wu, Li Feng, and Jinbo Song. 2018. Deep learning for fall detection: Three-dimensional CNN combined with LSTM on video kinematic data. *IEEE J. Biomed. Health Inform.* 23, 1 (2018), 314–323.
- [134] Peijun Zhao, Chris Xiaoxuan Lu, Bing Wang, Changhao Chen, Linhai Xie, Mengyu Wang, Niki Trigoni, and Andrew Markham. 2020. Heart rate sensing with a robot mounted mmWave radar. In *IEEE International Conference on Robotics and Automation (ICRA'20)*. IEEE, 2812–2818.
- [135] Kilin Shi, Tobias Steigleider, Sven Schellenberger, Fabian Michler, Anke Malessa, Fabian Lurz, Nicolas Rohleder, Christoph Ostgathe, Robert Weigel, and Alexander Koelpin. 2021. Contactless analysis of heart rate variability during cold pressor test using radar interferometry and bidirectional LSTM networks. *Scient. Rep.* 11, 1 (2021), 1–13.
- [136] Jian Gong, Xinyu Zhang, Kaixin Lin, Ju Ren, Yaoxue Zhang, and Wenxun Qiu. 2021. RF vital sign sensing under free body movement. *Proc. ACM Interact. Mob. Wear. Ubiqu. Technol.* 5, 3 (2021), 1–22.
- [137] Tianyue Zheng, Zhe Chen, Shujie Zhang, Chao Cai, and Jun Luo. 2021. MoRe-Fi: Motion-robust and fine-grained respiration monitoring via deep-learning UWB radar. In *19th ACM Conference on Embedded Networked Sensor Systems*. 111–124.

- [138] Zhe Chen, Tianyue Zheng, Chao Cai, and Jun Luo. 2021. MoVi-Fi: Motion-robust vital signs waveform recovery via deep interpreted RF sensing. In *27th Annual International Conference on Mobile Computing and Networking*. 392–405.
- [139] Teemu Vepsäläinen, Markku Laakso, Seppo Lehto, Auni Juutilainen, Juhani Airaksinen, and Tapani Rönnemaa. 2014. Prolonged P wave duration predicts stroke mortality among type 2 diabetic patients with prevalent non-major macrovascular disease. *BMC Cardiovasc. Disord.* 14, 1 (2014), 1–7.

Received 3 July 2023; revised 25 September 2023; accepted 5 October 2023